RSC Advances

PAPER

View Article Online
View Journal | View Issue

Cite this: *RSC Adv.*, 2025, **15**, 43523

Extending lead-free organic–inorganic semiconducting materials to new polymeric structures: 2,2′-bipyridinium iodoantimonate and quinoxalinium iodobismuthate

Chakib Hrizi, *[a] Monia Hamdouni, [a] Marwa Essid,[a] Mourad Nouiri,[b] Abderrahim Khatyr,[c] Michael Knorr, [c] Lydie Viau, [c] Annika Schmidt, [d] Carsten Strohmann [d] and Slaheddine Chaabouni[e]

We report on the synthesis, crystal structures and optoelectronic properties of two novel organic–inorganic group V iodometalates – (bpy-H)SbI_4 (**1**) and $(Qx\text{-}H)_2[BiI_4]_2\cdot CH_3OH$ (**2**) (bpy-H: 2,2′-bipyridinium; Qx-H: quinoxalinium). Crystals of both compounds were grown solvothermally using as starting reagents antimony(III) iodide and 2,2′-bipyridine, for **1**, and bismuth(III) iodide and quinoxaline, for **2**. Both compounds were structurally analyzed by single crystal X-ray diffraction at 100 K and their structures feature one-dimensional edge-sharing anionic chains of MI_6-octahedra, with short interchain I⋯I contacts giving rise to the possibility of three-dimensional charge transport capability. The cavities between the one-dimensional $[MI_4^-]_n$ chains are occupied by the rigid *N*-protonated organic amines – 2,2′-bipyridinium (bpy-H), for **1**, and quinoxalinium (Qx-H), for **2** – to balance the charge and stabilize the structures. The study of their supramolecular 3D structures assisted by a Hirshfeld surface analysis revealed that the latter are due to several types of intermolecular interactions, such as intermolecular hydrogen-bonding (H⋯I and H⋯O) and additional π⋯π and I⋯I contacts. Solid-state optical studies performed on powders and thin films were carried out and revealed that the materials display semiconductive optical band gap energies of around 2.17 eV, for **1**, and 2.03 eV, for **2**, which is encouraging for optoelectronic applications. The bulk crystals of **1** exhibit a broad dual-band emission which originates from both free excitons (FE) and self-trapped excitons (STE), as proven by its long lifetime (146.32 ns) and the temperature dependences of broadband emission. In contrast, bulk crystals of **2** exhibit broadband emission centred at 454 nm, common to the salt (Qx-H)Cl, originating from ligand-centered transition. These are proven by their short lifetimes (3.86 ns for **2** and 1.07 ns for (Qx-H)Cl).

Received 20th August 2025
Accepted 31st October 2025

DOI: 10.1039/d5ra06189j

rsc.li/rsc-advances

1. Introduction

Hybrid inorganic–organic metal halides have been largely explored for use in a variety of applications and devices including photovoltaics, light-emitting devices, photodetectors, and radiation detectors.[1–7] These compounds combine the high carrier mobilities and absorption coefficients of traditional inorganic semiconductors with the flexibility and processability of organic electronics within a single material.[4,5,7] A prominent group within the larger class are trivalent metal halide *p*-block materials, in particular, halogenido antimonates and bismuthates $[R_x(M_yA_z)]$ (where R = an organic cation; M = Sb(III) or Bi(III); A = Cl, Br, I; *x*, *y*, and *z* represent the stoichiometry). The latter have attracted attention as promising materials not only due to their higher stability[8] and low toxicity[9] compared to typical lead halide perovskites,[10] but also due to their interesting optical and electronic properties including luminescence, semiconductivity, photochromism, thermochromism, *etc.*,[11,12] as well as their fascinating structural topologies. Among them, halogenido antimonates/bismuthates (which have s^2 lone pairs) are receiving more attention in striving to find non-toxic materials and showing properties favorable for light harvesting. However, up to now, research on bismuth and antimony halide derivatives has not progressed significantly to achieve reasonable light-harvesting properties. Indeed, their photovoltaic

[a]*Research Unit Advanced Materials, Applied Mechanics, Innovative Processes, and Environment, UR22ES04, Higher Institute of Applied Sciences and Technology of Gabes, University of Gabes, Tunisia. E-mail: h_chakib1212@yahoo.fr*

[b]*Laboratory of Physics of Materials and Nanomaterials Applied at Environment, Faculty of Science of Gabes, University of Gabes, Tunisia*

[c]*Université Marie et Louis Pasteur, CNRS, Institut UTINAM (UMR 6213), F-25030 Besançon, France*

[d]*Anorganische Chemie, Technische Universität Dortmund, Otto-Hahn Straße 6, 44227 Dortmund, Germany*

[e]*Laboratoire des Sciences des Matériaux et de l'Environnement, Faculté des Sciences de Sfax, Université de Sfax, BP 1171, 3000 Sfax, Tunisia*

efficiency is only 4%.[13,14] Meanwhile, they exhibit favorable properties for solar light harvesting. This is explained by the fact that they have active lone electron pairs in their valence shells, polarizable electron layers and band dispersion due to strong spin–orbit coupling.[15] In this context, bandgap engineering is at the heart of the development of halogenido antimonates/bismuthates with low bandgaps and capable of solar light harvesting.

In the oxidation state +3, the anionic subnetworks of halogenido antimonates and bismuthates are constituted of distorted $[M_yA_z]^{(z-3y)-}$ octahedra, which may be isolated or condensed by corner-, edge-, or face-sharing of the polyhedra, forming thus various different arrangements (see Fig. 1). We find in the literature 0D clusters such as $[MA_6]^{3-}$, $[M_2A_9]^{3-}$, $[M_2A_{10}]^{4-}$, $[M_3A_{11}]^{2-}$, $[M_3A_{12}]^{3-}$, $[M_4A_{16}]^{4-}$, $[M_4A_{20}]^{8-}$, $[M_5A_{18}]^{3-}$, $[M_6A_{22}]^{4-}$, $[M_7A_{24}]^{3-}$, $[M_8A_{28}]^{4-}$ and $[M_{10}A_{34}]^{4-}$,[16–22] 1D chains such as $[MA_4]^-$, $[MA_5]^{2-}$, $[M_2A_7]^-$ and $[M_3A_{10}]^-$[23–27] as well as 2D extended network, $\left[M\frac{2}{3}I_4\right]_n^{2-}$, in the layered perovskite $[H_2AEQT]M_{2/3}I_4$ (M = Sb(III) or Bi(III))[28] (Fig. 1).

The optical and opto-electronic properties of halogenido antimonates and bismuthates are directly influenced by the dimensional reduction concept or by the variation in the anions size of the same dimensionality.[20,29,30] For example, changing from a "2D" network in SbI_3 parent or in the layered $Cs_3Sb_2I_9$ (ref. 31) structure to a "0D" anion in $(H_2NMe_2)_3SbI_6$ (ref. 16) leads to an increase in the optical band gap from 2.10 or 2.05 to 2.30 eV. Also, optical band gaps of halogenido antimonates and bismuthates vary considerably in compounds containing the same type of anion but different cations. For example, optical band gaps between 1.79 and 2.41 eV have been reported for compounds containing $[SbI_5]^{2-}$ anions as *cis*-connected octahedra forming a zigzag chain.[32–35] These are due to differences in crystal packing which leads to differences in the degree of distortion of the $[SbI_6]^{3-}$ octahedra. These distortions are believed to have a distinct influence on the optical bandgap in halogenido antimonates materials.

Due to the low-dimensionality of halogenido antimonates and bismuthates, quantum confinement effects appear, predicting a smaller band gap for thicker or larger anions. Thus, stable excitons with high binding energies appear, and they are confined in the inorganic structure giving rise to interesting optical and optoelectronic properties.[18,19,23] Indeed, as a result of dimensionality reduction, the deformable anionic subnetwork and structural confinement facilitate the confinement of free excitons (FE) in the deformed anionic polyhedron, thereby promoting the formation of self-trapped excitons (STEs), which typically exhibit broadband emission even covering the entire visible spectrum.[36,37] Moreover, the coexistence of FEs and STEs allows low-dimensional metal halide perovskites (M = Bi, Sb) to attract dual-band or multi-band emission behaviors, resulting in white emission.

Here, we present the organic–inorganic halogenido metalates (Cat)MI_4 (Cat = 2,2′-bipyridinium (**1**), quinoxalinium (**2**); M = Sb (**1**), Bi (**2**)) which both exhibit supramolecular pseudo-3D structures *via* I···I contacts between $[MI_4^-]_n$ polyhedra. For this work, we have chosen SbI_3 and BiI_3 (i) due to their better chemical and thermal stabilities compared to $Cs_3Bi_2I_9$ (ref. 8) and (ii) because they are stable to oxidation in the presence of iodine. As for the R-site of $R_x(M_yA_z)$, two rigid aromatic amines, such as 2,2′-bipyridine and quinoxaline, were used to occupy this site. The choice of these aromatic amines is explained by the ability of their protonated cations to function as a structure-oriented template. Both compounds exhibit excellent semiconductor properties, including low band gaps of 2.17 eV for **1** and 2.03 eV for **2**, and dual-band emission behavior for **1**. The structural, optical and optoelectronic properties were investigated, making (bpy-H)SbI_4 (**1**) and $(Qx\text{-}H)_2[BiI_4]_2\cdot CH_3OH$ (**2**) promising candidates for optoelectronic applications.

2. Results and discussion

2.1 Synthesis

All compounds were synthesized *via* a solvothermal method in good or very good yield. Single crystals of (bpy-H)SbI_4 (**1**) were grown from a mixture of SbI_3 and 2,2′-bipyridine using acetonitrile as the reaction solvent. The synthetic details are summarized in Scheme 1. In the absence of an added acid, charge balance for the SbI_4^- anion is provided by 2,2′-bipyridinium, which becomes protonated under the specific reaction conditions to yield $(bpy\text{-}H)^+$.

While the formation of polynuclear iodometalate anions during reaction with *N*-donating ligands and without the addition of an acid is not uncommon, the protonation of these ligands in polar solvent such as MeCN, THF, H_2O, MeOH or EtOH has also been reported and deserves some comments.[20,38,39] For example, crystals of $(2,2'\text{-}Hbpy)_4Bi_6I_{22}$ were grown solvothermally in an ethanol/water solvent mixture using BiI_3, 2,2′-bipyridine and RuI_3 (as additional iodide source) as starting materials.[38] Treatment of BiI_3 with Z-Py-S(CH_2CH=

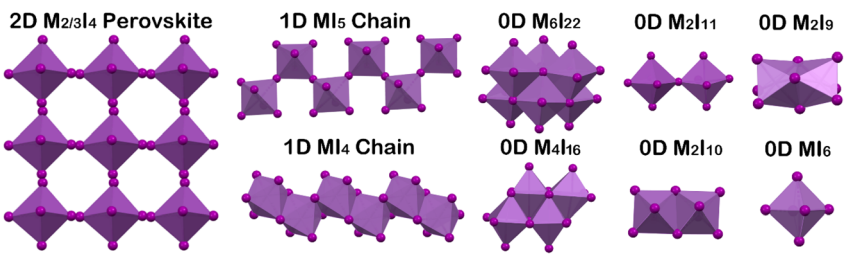

Fig. 1 Structural versatility of octahedral metal iodides (M = Sb or Bi): from 2D perovskite to low-dimensional metal iodides.

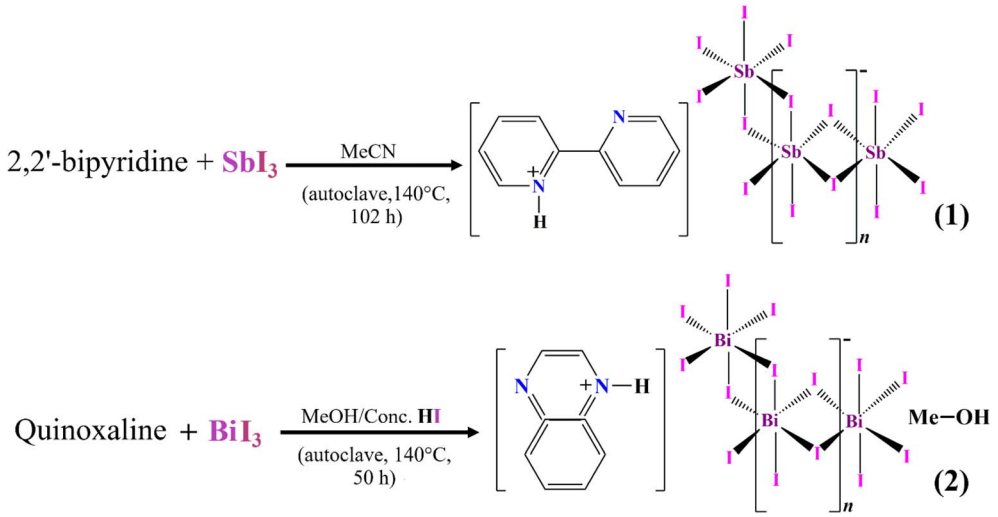

Scheme 1 Preparation of compounds **1** and **2**.

$CHCH_2$)S-Py in MeOH is reported to afford the iodobismuthate salt $(C_{14}H_{15}S_2N_2)_2(C_9H_{10}SN)_2Bi_4I_{16}$.[20] Also, the reaction between SbI_3, and an excess of dmpu (dmpu = *N*,*N*′-dimethylpropylene urea) in THF afforded, after repeated crystallisations, crystals of the complex $(C_5NH_6)_2(H(dmpu)_2)Sb_2I_9$.[39] To check the reproducibility of this outcome, we repeated the reaction summarized in Scheme 1 under similar conditions. SC-XRD analysis of the isolated orange crystals revealed that the material was identical to that of (bpy-H)SbI_4 (**1**), highlighting the impact of the MeCN solvent on the protonation of the 2,2′-bipyridine.

The solvothermal reaction between BiI_3, quinoxaline and HI in methanol resulted in the growth of dark-red crystals of (Qx-H)$_2$[BiI_4]$_2\cdot CH_3OH$ (**2**). The latter contains an infinite BiI_4^- chain that is charge-balanced by protonated quinoxaline cations (Scheme 1). Recently, we reported on the reaction of $Bi(NO_3)_3$ with quinoxaline in the presence of HI in an acetone/H_2O solvent mixture.[40] To our surprise, the 1D-polymeric iodobismutate $[(Qx\text{-}H^+)BiI_4]_n$ did not constitute the main product but was isolated in only about 20% yield. The main product was a highly nitrated quinoxaline derivative, namely 5,6,7,8-tetranitro-1,2,3,4- tetrahydroquinoxaline-2,3-diol, which has been isolated in 55% yield. The two isolated salts, $[(Qx\text{-}H^+)BiI_4]_n$ and compound **2**, have at first glance the same composition. However, a closer look reveals that the products are in reality quite different concerning shape and colour of the crystals, crystal system (*Cc vs.* $P\bar{1}$), lattice parameters (see below). This isomerism highlights the impact of the synthesis protocol on the structural parameters. Under the chosen solvothermal synthesis conditions, the solvent molecules were inserted into crystalline structure.[17,18,27] Indeed, under high temperature and pressure, methanol molecules become trapped within the pores of the structure while forming hydrogen bonds with the protonated amine.

The reaction leading to the final product involves the *in situ* formation of the anionic species from the neutral starting reagent MI_3 (M = Bi or Sb). However, these anionic structures can be related to each other by the dimensional reduction concept. Indeed, the one-dimensional $(MI_4^-)_\infty$ chain can be obtained by excision of the 2D layer of the parent MI_3 structure by adding an equivalent of I^- to MI_3 (see Fig. 2). By adding another I^-, further dimensional reduction of this chain can lead in its turn to a half of an $(M_2I_{10})^{4-}$ edge-shared octahedra dimer, while adding another additional equivalent of I^- can ultimately yield the MI_6^{3-} isolated octahedron (see Fig. 2). Tulsky *et al.* suggest that these additional iodide ligands terminate the M–X–M bonds in the extended array of solid MX_3, thereby affecting a reduction in dimensionality.[30]

Ground samples of compounds **1** and **2** were analyzed by powder X-ray diffraction (PXRD). For each of the two compounds, the experimental PXRD pattern corresponds well to the simulated one, confirming the purity and homogeneity of

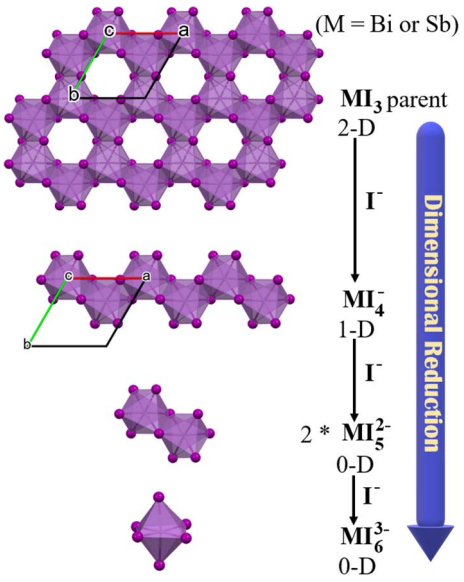

Fig. 2 Anionic networks, $[MI_4]^-$, $[M_2I_{10}]^{4-}$ and $[MI_6]^{3-}$, derived from the parent BiI_3/SbI_3 (2-D) compounds, illustrating the concept of dimensional reduction.

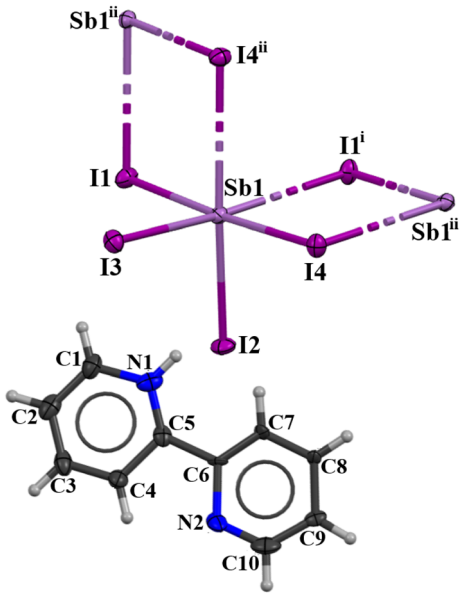

Fig. 3 The asymmetric part of the unit cell of crystals **1**, showing the atom-numbering scheme. Dashed lines represent bonds to adjacent symmetry-generated atoms (symmetry codes: (i) x, $1-y$, $\frac{1}{2}+z$; (ii) x, $1-y$, $\frac{1}{2}+z$). Displacement ellipsoids are drawn at the 50% probability level and H atoms as small spheres of arbitrary radii.

the phases. The PXRDs are shown in the SI (Fig. S1 and S2). Since the PXRDs were recorded at 298 K and the SC-XRD at 100 K, the matching excludes also the occurrence of phase-transitions in this temperature interval. Furthermore, the DSC curves obtained for crystals **1** and **2** during cooling and heating analyses show no anomalies (Fig. S3 and S4), corroborating this hypothesis.

2.2 Single crystal structures

The solid-state structures of **1** and **2** compounds were elucidated by single-crystal X-ray diffraction (SC-XRD) studies at 100 K.

Compound **1** crystallizes in the *Cc* acentric space group, and the asymmetric part of the unit cell is shown in Fig. 3.

The crystal structure of **1** consists of a framework of one-dimensional $(SbI_4^-)_\infty$ chains of edge-sharing $[SbI_6]^{3-}$ octahedra extended along the *c*-axis, separated by a network of $(bpy\text{-}H)^+$ organic cations. The crystal packing of **1** is shown in Fig. 4. $(SbI_4^-)_\infty$ chains are a well-known anion type in the chemistry of iodido antimonates and several examples are known with geometric characteristics similar to those found in compound **1**.[41–45] Bond lengths are within expected ranges (see Table 1), showing a greater tendency towards distorted octahedral environment around the antimony center. The inorganic chain structure for **1** is derived from a single crystallographically

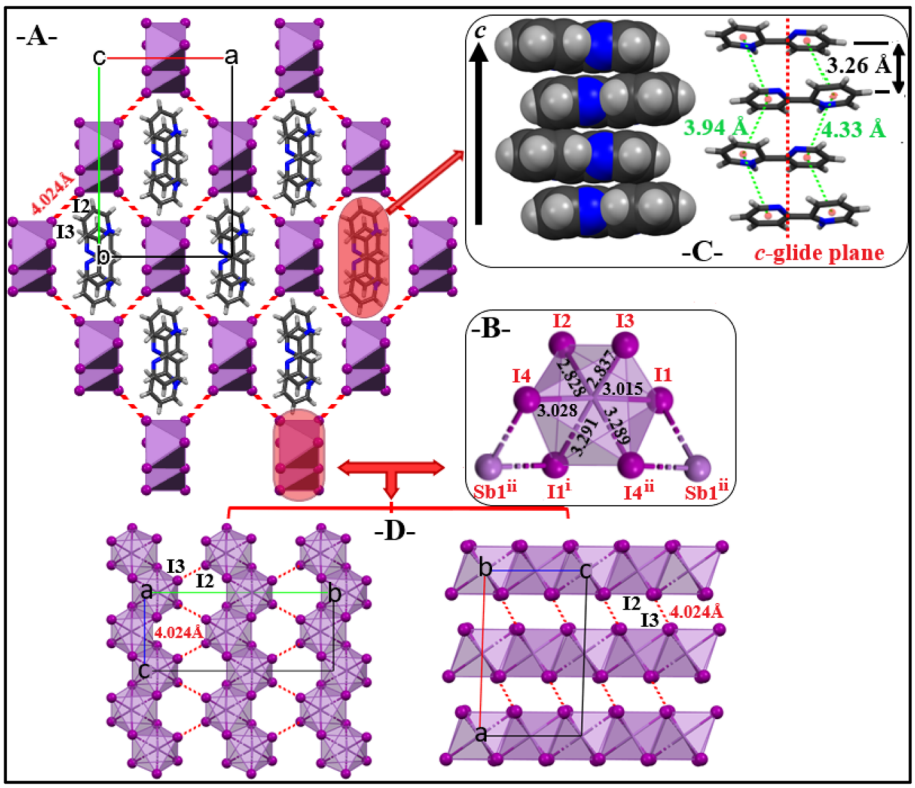

Fig. 4 Crystal structure of **1**: (A) view of the crystal packing along [001]. Pseudo-3D frameworks formed *via* I···I contacts (dashed) between the $[SbI_4^-]_n$ chains; (B) the coordination of $[SbI_6]^{3-}$ octahedron; (C) space-filling (left) and ball and sticks (right) representations of stacks of $(bpy\text{-}H^+)$ entities along the *c*-axis; (D) crystallographic packing diagrams showing only the anionic 1D network with interchain I···I interactions (in red), which connect the anions into a 2-D arrays along *a*- and *b*-axes (the cations are omitted). Symmetry codes: (i) x, $1-y$, $\frac{1}{2}+z$; (ii) x, $1-y$, $-\frac{1}{2}+z$.

Table 1 Selected interatomic distances (Å) and angles (deg) in the $[SbI_6]^{3-}$ octahedron of **1**[a]

Bond length (Å)		Bond angles (°)	
Sb–I_1	3.015 (1)	I_1–Sb_1–I_2	88.67 (3)
Sb_1–I_2	2.828 (9)	I_1–Sb_1–I_3	93.85 (3)
Sb_1–I_3	2.837 (9)	I_1–Sb_1–I_4	176.640 (8)
Sb_1–I_4	3.028 (1)	I_1–Sb_1–I_4^{ii}	87.343 (1)
Sb_1–I_1^{i}	3.291 (1)	I_1^{i}–Sb_1–I_3	172.543 (1)
Sb_1–I_4^{ii}	3.289 (1)	I_2–Sb_1–I_3	94.957 (7)
		I_2–Sb_1–I_4	93.69 (3)
		I_2–Sb_1–I_4^{ii}	173.046 (3)
		I_3–Sb_1–I_4	88.33 (3)
		I_1–Sb_1–I_1^{i}	90.471 (1)
		I_1^{i}–Sb_1–I_2	91.211 (1)
		I_1^{i}–Sb_1–I_3	90.995 (1)
		Sb_1–I_1–Sb_1^{ii}	92.885 (1)
		Sb_1–I_4^{ii}–Sb_1^{ii}	92.679 (1)

[a] Symmetry codes: (i) x, $1-y$, $\frac{1}{2}+z$; (ii) x, $1-y$, $-\frac{1}{2}+z$.

independent SbI_6 octahedron (Fig. 4B), with Sb–I bond lengths in the range from 2.828(9)–3.291(1) Å. Out of three pairs of opposite Sb–I bonds two involve one bridging and one terminal bond, while the third involves two bridging bonds. The longest Sb–I bonds (3.289(1) and 3.291(1) Å) are characteristic of the bridging iodine atoms of the first two pairs. The shortest bonds (2.828(9) and 2.837(9) Å) are characteristic of the terminal iodine atoms opposite to the bridging. Two bridging Sb–I bonds *trans* to each other have intermediate lengths (3.015(1) and 3.028(1) Å). The average Sb–I bond lengths (3.0478 Å) are shorter than the sum of van der Waals radii of their corresponding atoms (Σr_{VDW}(Sb–I) = 4.04 Å; r_{VDW}(Sb) = 2.06 Å, r_{VDW}(I) = 1.98 Å) and are in the same order to those reported in $[C_6H_9N_2O]SbI_4$ (ref. 45) (3.03 Å on average) and $[C_4H_7N_2]SbI_4$ (ref. 43) (3.04 Å on average). The I–Sb–I angles to each other fall in the range 87.343(1)° to 94.959(1)° for *cis* and 172.543(1)° to 176.638(1)° for *trans* arrangements (see Table 1). As described by Brown's model,[46] this distorted octahedral coordination geometry could be explained as the stereochemical activity of the Sb(III) lone electron pair ($5s^2$ orbital), which moves in the Sb–$I_{bridging}$ direction (trans to the Sb–Sb vector) to minimize the Sb···Sb interactions. This behavior is in agreement with other iodido metalates materials containing 0D frameworks or similar 1D chains.[20,23,40]

The significant feature of **1** is its crystal packing (Fig. 4). Its crystal structure can nominally be viewed as consisting of alternating layers of SbI_4^- chains and (bpy-H^+) cations, stacked along the [001] crystallographic direction. The spaces between the infinite inorganic chains are occupied by the (bpy-H) moieties. There is one unique 2,2′-bipyridinium molecule in the asymmetric unit and its atomic numbering scheme is presented in Fig. 3. In the title compound, the two pyridinium and pyridine rings built up by (C1, C2, C3, C4, C5, N1) and (C6, C7, C8, C9, C10, N2) have almost the same degree of flatness (rms deviations of fitted atoms equal to 0.0363(2) and 0.0305(2), respectively) with a dihedral angle between these two planes which is 3.16(2)°. The cations form hydrogen bonds with the iodine atoms of the (SbI_4^-) anions and reveal stacking-like arrangement. The axes of these stacks are arranged parallel to the *c*-glide plane which are in turn placed perpendicular to the [010] crystallographic direction at $y = 1/2$. The values of the interplanar (3.269(1) Å) and intercentroid (3.940(1) Å and 4.336(1) Å) distances between parallel (bpy-H) rings indicate rather weak π–π arrangement. The geometry of the π–π stacks is presented in Fig. 4C. In the channels between the stacks the anionic sublattice is located and the interatomic Sb_1–Sb_1^{ii} axis is parallel to the *c*-direction. It is connected to the 2,2′-bipyridinium cations by weak N/C–H···I type hydrogen bonds (see Fig. S3). Numerous H···I^- interactions in the range of 2.88–3.23 Å are found between each I and H atom of the 2,2′-bipyridinium cations (the sum of van der Waals radii of I and H is 3.18 Å). A detailed summary of the weak interactions is tabulated in Table S2.

As a result of the hydrogen bonding interactions, the infinite inorganic chains, that extend along the *c*-axis of the structure, are brought into close contact while forming of a pseudo-two-dimensional array of SbI_4^- chains *via* I···I interactions. Close interactions between iodides on adjacent chains within a layer include I(3)···I(2)′ (′: $-\frac{1}{2}+x, \frac{1}{2}-y, -\frac{1}{2}+z$) with a distance d(I(3)···I(2)′) = 4.024 Å which is much shorter than twice the ionic radius for the iodide ion (2.2 Å).[47] Also, the I(3)···I(2)′ distance is slightly greater than the sum of van der Waals radii of two I atoms (3.96 Å) indicating that the chains are in close contact within the inorganic layers.

When viewed along the [−110] crystallographic direction, close interactions between iodides on adjacent chains include I(2)···I(3)′ [d(I(2)···I(3″)) = 4.024 Å; ″: $\frac{1}{2}+x, \frac{1}{2}-y, \frac{1}{2}+z$]. These interactions extending along both cell diagonal directions in the *ab* plane, producing a degree of 3D connectivity which leads to a more pseudo-three-dimensional packing of the array of chains (Fig. 4D). In comparison with crystalline I2, reported by Van Bolhuis *et al.*, the intermolecular I···I distances in-layer are 3.50 Å and 3.97 Å, while those between layers are 4.27 Å.[48] The 3D framework of antimony-iodide perovskite may have an interesting consequence in terms of dimensionality-dependent optical properties, *i.e.* quantum confinement behavior.[17,18,49] Furthermore, it is essential to potentially extend the electronic conductivity pathways which potentially achieve efficient isotropic charge transport in the solid material.[23,50] This is the first example of a Sb-based perovskite with a pseudo-3D structure, which is formed by connecting [SbI_4^-] chains *via* adjacent I···I interactions. It should be noted that the packing form of $[SbI_4]^-$ chains and (bpy-H)$^+$ in the crystal of **1** resembles the (Qx-H)BiI_4,[40], $(C_5H_6N)BiI_4$ and $(C_6H_8N)BiI_4$ (ref. 51) materials with pseudo-3D structures.

To study the effect of halide type on the structure and the crystal packing, we examined and compared in detail the two structures (2,2′-bipyH)$_4[Sb_4X_{20}]$ with X = Br[52] or Cl[53] (see Fig. S6 in SI).[52,53] This type of structure is rare; it was described solely for chlorobismuthates(III),[54,55] chloroantimonates(III)[53,56] bromoantimonates(III)[52] and for antimony(III) mixed bromide chlorides.[57] The zero-dimensional $[Sb_4X_{20}]^{8-}$ anion consists of four octahedral {SbX_6} moieties sharing two out of six halide ligands so that the Sb atoms form a slightly distorted square

(see Fig. S6). Compounds $(2,2'\text{-Hbpy})_4[Sb_4X_{20}]$ (X = Br or Cl) are essentially isostructural despite the different nature of their halogens. This is reflected in the similarity of the unit cell dimensions and space groups. In both compounds the geometry of the tetrameric anions $[Sb_4X_{20}]^{8-}$ is essentially identical and the similarity of the crystal packing is notable (see Fig. S6). Furthermore, they differ only slightly in the Cl···Cl and Br···Br interactions between the $[Sb_4X_{20}]^{8-}$ tetramers. Interestingly, the tetrameric anions $[Sb_4X_{20}]^{8-}$ in the two structures are separated from each other with the closest Br···Br and Cl···Cl distances of 3.573 and 3.576 Å for $[Sb_4Br_{20}]^{8-}$ and 3.447 and 3.608 Å for $[Sb_4Cl_{20}]^{8-}$ (see Fig. S6). These distances are obviously shorter than the sum of two ionic radii of Br^- (1.96 × 2 Å) and Cl^- (1.81 × 2 Å), extending the anionic network along both the *a*- and *c*-axes of all two compounds. This can be considered as producing a degree of 3D connectivity in the materials.

Compound **2** crystallizes in the triclinic crystal system with the $P\bar{1}$ space group, the lattice parameters are shown in Table 5. It should be noted that $[(Qx\text{-}H^+)BiI_4]_n$,[40] similar to **2**, crystallizes in a monoclinic crystal system with the non-centrosymmetric space group *Cc* with the following lattice parameters: a = 15.2703(8) Å, b = 14.2742(8) Å, c = 7.4001(4) Å, β = 117.674(2)° and Z = 4. The asymmetrical unit of **2** consists of one independent quinoxalinium cation, one bismuth atom, and four iodides that are located in general positions. It also contains half of the MeOH solvate molecule (Fig. 5). The BiI_4 unit generates a one-dimensional iodobismuthate $[BiI_4^-]_n$ chain, *via* Bi_1–μ_2-I_1–Bi_1^{i} and Bi_1–μ_2-I_2–Bi_1^{ii} bridges [(i): $-x+1$, $-y+2$, $-z+1$; (ii): $-x$, $-y+2$, $-z+1$], to build the compound **2**.

The crystallographic packing for **2** along the *a*-direction is presented in Fig. 6A, displaying an inorganic framework built by $[BiI_4]_n^{n-}$ anionic chains with Qx-H^+ arranged around to balance the charge and are located within channels extending through the *a*-axis of the structure in parallel with the inorganic sublattice (Fig. 6A). The $[BiI_4]_n^-$ chains are formed from edge sharing individual $[BiI_6]^{3-}$ octahedra, leading to 4 bridging and 2 terminal *cis*-related iodine atoms. As expected, the Bi–I bond distances involving terminal iodides (2.9152(3) and 2.9326(3) Å) are shorter than those involving shared iodides (3.0691(3)–3.2872(3) Å) in each BiI_6 octahedron (Fig. 6B and Table 2). This range of Bi–I bond lengths (3.098 Å on average) are shorter than the sum of van der Waals radii of their corresponding atoms (Σr_{VDW}(Bi–I) = 4.05 Å; r_{VDW}(Bi) = 2.07 Å, r_{VDW}(I) = 1.98 Å) and fall in the range of other reported bismuth-containing iodides with similar 1D $[BiI_4]_n^-$ chain frameworks, such as $(NH_3(CH_2)_2NH_3)[BiI_4]_2\cdot 4H_2O$ (3.092 Å on average)[58] and (naphtylammonium)BiI_4 (3.088 Å on average).[23] $(Qx\text{-}H)_2[BiI_4]_2\cdot CH_3OH$ (2) structure exhibits a disimilar range of Bi–I bond lengths (average of 3.0982 Å) compared with (Qx-H)BiI_4 (average of 2.9665 Å).[40] The largest changes in Bi–I bond lengths involve the two terminal Bi–I bonds (by *ca.* 0.18–0.262 Å) and the two bridging Bi–I bonds *trans* to each other (by *ca.* 0.141–0.17 Å). The bond angles for *cis* I–Bi–I range from 82.88(2)° to 95.48(8)° while the *trans* I–Bi–I angles are in the range of 171.98(8)° to 174.52(8)°, and the $I_{bridging}$–Bi–$I_{bridging}$ angles in each BiI_6 octahedron are generally more deviated from the ideal angle (90° and 180°) than those of $I_{terminal}$–Bi–$I_{terminal}$

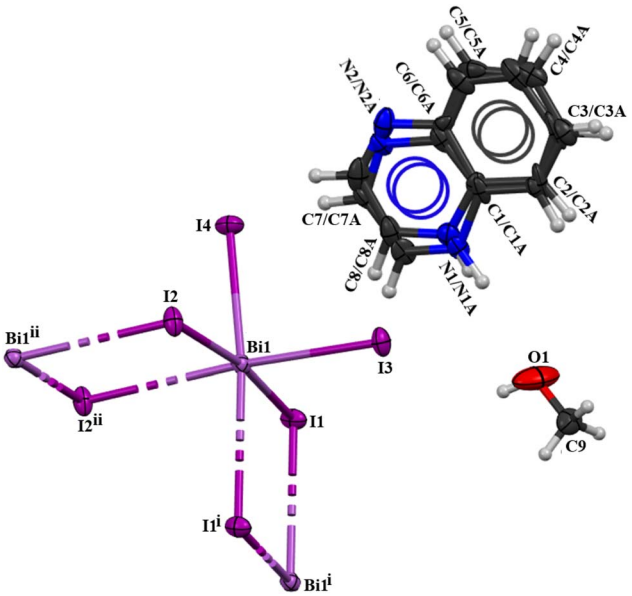

Fig. 5 The asymmetric part of the unit cell of crystals **2**, showing the atom-numbering scheme. Dashed lines represent bonds to adjacent symmetry-generated atoms (symmetry codes: (i) $-x+1$, $-y+2$, $-z+1$; (ii) $-x$, $-y+2$, $-z+1$). Displacement ellipsoids are drawn at the 50% probability level and H atoms as small spheres of arbitrary radii.

(see Table 2). The deviation of the geometric parameters indicates that the BiI_6 octahedron is distorted and this deformation could be interpreted as the stereochemical activity of the Bi(III) lone electron pair ($6s^2$ orbital), which is a common characteristic of iodobismuthates.[19,23,40,58]

The quinoxalinium cation, $[Qx\text{-}H]^+$, is disordered over two close positions (suffix A for the less occupied part), which gives two groups of C and N atoms slightly shifted from each other (see Fig. S7). The main geometric features of the $[Qx\text{-}H^+]$ cation, such as bond lengths and angles (see Table S3), are consistent with those reported for other structures containing quinoxalinium cations ((Qx-H)BiI_4,[40] (Qx-H)$_4Bi_2Cl_{10}$,[59] (Qx-H)$_4Sb_2Cl_{10}$,[21] and (Qx-H)$_4[H_2(FeCN_6)]_2Qx$[60]). As shown in the packing structure (Fig. 6A), the quinoxalinium cations fill channels between the inorganic chains. Besides, these organic cations are simultaneously connected to methanol molecules and 1D chains through N–H···O and N–H···I hydrogen bonds in the [131] direction (see Fig. S8). Moreover, the Qx-H^+ cations are located one below the other, and such a geometry is stabilized by π···π stacking interactions (see Fig. 6C) (perpendicular interplanar spacings of 3.78 Å, 3.82 Å, 4.2 Å and 4.38 Å at 100 K) that propagate along the [100] direction.

Interestingly, short interchain I···I interactions between adjacent $[BiI_4]^-$ anionic networks can been seen along both the *a*- (4 Å) and *b*-axes (4.04 Å and 4.25 Å) (Fig. 6D and 6E). These distances are significantly shorter than the sum of the ionic radii of two I^- anions (4.40 Å) and contribute strongly to the production of a degree of 3D connectivity in the material. Viewing at the structure along the crystallographic [100] direction (Fig. 6D), we can see that $[BiI_4]^-$ anionic chains are connected to each other *via* I_{bridg}···I_{term} (4.25 Å) and I_{term}···I_{term}

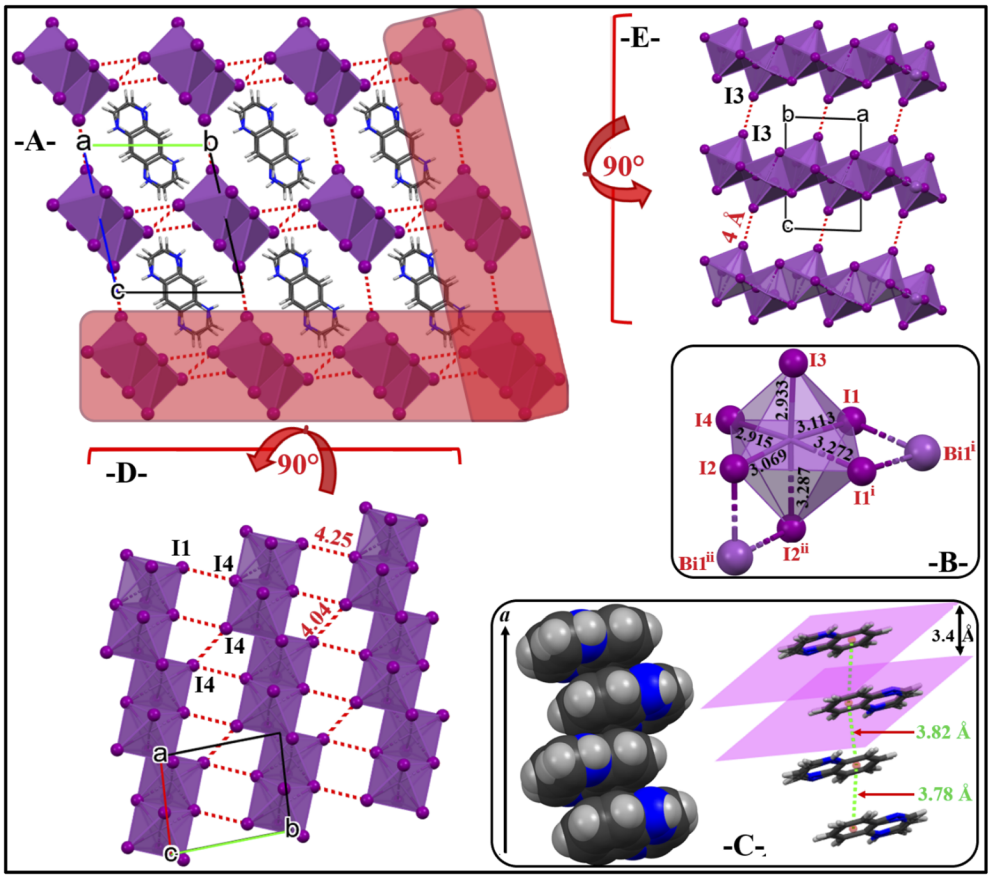

Fig. 6 Crystal structure of **2**: (A) view of the crystal packing along [100]. Pseudo-3D framework formed *via* I···I contacts (dashed) between the $[BiI_4^-]_n$ chains (MeOH molecules are omitted for clarity); (B) the coordination of $[BiI_6]^{3-}$ octahedron; (C) space-filling (left) and ball and sticks (right) representations of stacks of (Qx-H$^+$) entities along the *a*-axis; [001] (D) and [010] (E) views highlighting the I···I interactions (in red), which connect the anions into a 2-D arrays (cations/solvent are omitted for clarity). Symmetry codes: (i) $1-x, 2-y, 1-z$; (ii) $-x, 2-y, 1-z$.

Table 2 Selected interatomic distances (Å) and angles (°) in the $[BiI_6]^{3-}$ octahedron of **2**[a]

Bond length (Å)		Bond angles (°)	
Bi_1–I_1^i	3.2724 (3)	I_1–Bi_1–I_1^i	87.708 (7)
Bi_1–I_1	3.1129 (3)	I_1–Bi_1–I_2^{ii}	86.690 (7)
Bi_1–I_2	3.0691 (3)	I_1^i–Bi_1–I_2^{ii}	82.887 (7)
Bi_1–I_2^{ii}	3.2870 (3)	I_2–Bi_1–I_1	172.687 (7)
Bi_1–I_3	2.9328 (3)	I_2–Bi_1–I_1^i	88.698 (7)
Bi_1–I_4	2.9154 (3)	I_2–Bi_1–I_2^{ii}	86.547 (7)
		I_3–Bi_1–I_1^i	92.162 (8)
		I_3–Bi_1–I_1	95.477 (8)
		I_3–Bi_1–I_2	91.020 (7)
		I_3–Bi_1–I_2^{ii}	174.525 (8)
		I_4–Bi_1–I_1^i	171.995 (8)
		I_4–Bi_1–I_1	88.643 (7)
		I_4–Bi_1–I_2^{ii}	89.792 (8)
		I_4–Bi_1–I_2	94.110 (8)
		I_4–Bi_1–I_3	95.278 (8)
		Bi_1–I_1–Bi_1^i	92.292 (7)
		Bi_1–I_2–Bi_1^{ii}	93.453 (7)

[a] Symmetry codes: (i) $-x+1, -y+2, -z+1$; (ii) $-x, -y+2, -z+1$.

(4.04 Å) interactions to form a layer. The chains in the layer are arranged in AAAA mode along the [010] direction. The layers are stacked with each other along the [001] direction per AAAA mode (Fig. 6E) *via* $I_{term}\cdots I_{term}$ interactions (4 Å between the layers). From the electronic perspective, the pseudo-3D perovskite structure built from bismuth iodide is desirable for efficient isotropic charge transport in the solid material.

2.3 Hirshfeld surface analysis and fingerprint plots

The supramolecular features of compounds **1** and **2** were performed in a visually appealing and thorough manner using Hirshfeld surface (HS) analyses both for the anionic and the cationic units. In the discussion (see below), the scale of the properties mapped onto the Hirshfeld surface varies as follows: shape index is always mapped in the Hirshfeld surface between −1.0 (red) and +1.0 Å (blue), d_{norm} between −0.545 (red) and 1.765 Å (blue), d_e, mapped over the range −1.0 (red) and +1.0 Å (blue) and curvedness mapped between −4 and 4 Å. As well, decomposed fingerprint (FP) plots, constructed by plotting d_e against d_i simultaneously, were generated to provide detailed and quantified intermolecular interactions' views (Fig. S9 and S10) to reinforce impressions gained from the surfaces themselves. The decomposition of fingerprint plots enables to separate contributions from different interaction types, which commonly overlap in the full fingerprint.

For compound **1**, (Hbpy)SbI_4, as previously noted, hydrogen bond interactions between $(2,2'\text{-Hbpy})^+$ cations and $(SbI_4)^-$ anions were found to be dominant within the solid-state structure. Such interactions participate rather in the generation of a link between organic and inorganic molecules, strengthening the structural cohesion. In fact, N–H···I and C–H···I interactions manifest themselves on the cationic Hirshfeld surfaces mapped through d_e as significant broad convex bright-red depressions, appearing at the ends of the organic molecules, perpendicular to the N–H···I and C–H···I vectors, comprising 40% of the total Hirshfeld surface area of cationic molecule, highlighting the donor character played by those latters (see the top-right of the colored part in the middle of Fig. S9). Such H···I contacts are shown up in the organic units' 2D-fingerprint plot as a specific sharp spike (appointed as **1** in Fig. S9), characteristic of strong hydrogen bonds,[61] with $d_e + d_i \sim 2.8$ Å, appearing in the upper part of the FP (where $d_e > d_i$), underlining the donor caracter previously described.

In return, hydrogen bond acceptor regions appear above the I atoms, on anionic Hirshfeld surfaces mapped through d_e, with exactly the opposite curvature shape, plainly dotted with series of red concave depressions, comprising 73.9% of the total Hirshfeld surface area of anionic molecule and emphasizing the acceptor character played by inorganic molecules (see the bottom-right of the colored part in the middle of Fig. S9 and 7a). On the inorganic units' 2D-fingerprint plots, such I···H contacts are viewed as a sharp spike (appointed as **2** in Fig. S9), characteristic of strong hydrogen bonds, with $d_e + d_i \sim 2.8$ Å, appearing in the lower part of the anionic unit FP (where $d_e < d_i$), emphasizing the acceptor one (**1** in Fig. S9).[62] The broadness of the spikes **1** and **2** may be related to the presence of two different types of H···I contacs, namely N–H···I and C–H···I.

As previously noted, all the surfaces have been mapped over the same range of d_e. So that, the size and the colour of these regions are directly related to the closeness of the atom–atom contacts, which is often taken as synonymous with the strength of the individual hydrogen bond. Series of contacts have been detected as well between organic molecules themselves displaying different characteristic ranges of d_e and d_i. As shown on the top of the Fig. S9, the π···π stacking interaction is shown as a small part which comprises 7.3% of the total Hirshfeld surface area of the molecule. The proportion of π···N/N···π interactions also comprises 5.3% in 2D graph. Except its significant contribution in the creation of hydrogen bonds, hydrogen atoms are found to be involved in other interactions of type N···H/H···N, C···H/H···C and H···H with the proportions of respectively 4, 19.4 and 19.8%.

For anionic units, as shown on the decomposed Hirshfeld surfaces presented at the bottom of the Fig. S9, additional interactions came into play. In fact, Sb···I interactions were found to be present on the Hirshfeld surface mapped according to the shape index as nearly flat yellow regions largely green, perpendicular to the bonds created between Sb atom and the bridging iodine ones (I_1, I_1^{i}, I_4 and I_4^{ii}) (see description section), with a relative contribution of 11.7%. This result supports that each of Sb units makes a related bridge with the central Sb *via* previously noted bridging iodine atoms. Such interaction scheme develops parallel to the crystallographic *c* axis to give rise to one-dimensional (1-D) chains of edge-shared SbI_6 polyhedra. Besides, another intermolecular interaction of interest in this level is the I···I contact, with a relative contribution of 8.2%. Its importance lies in the substantial role it plays in the formation of the three-dimensionality of the structure. Fig. 7c illustrate the crystal-packing diagram of anionic units' curved surfaces, showing how the location of adjacent chains influences arrangement type involved in the creation of the structural framework. In fact, those latter are arranged in parallel chains along *a* axis of the crystal structure, while producing, through these I···I interactions, a three-dimensional stacking of the chain network. The presented areas are supportive to the observed intermolecular interactions described in previous sections.

Compound **2**, $(Qx\text{-}H)_2[BiI_4]_2\cdot CH_3OH$, shows features that are remarkably similar to those observed for compound **1**. Each Bi atom is connected to its neighboring Bi *via* bridging iodine atoms (I_1, I_1^{i}, I_2 and I_2^{ii}), generating one-dimensional iodobismuthate $[BiI_4^-]_n$ chains of edge-shared BiI_6 polyhedra, developing along *a*-axis. A such structural design is achieved through the presence of I···Bi intermolecular interactions. On the Hirshfeld surface made by shape index function, those latters are shown to be nearly flat yellow regions largely green with a relative contribution of 13.2% (see the bottom-right of the Fig. S10). The resulting framework displays channels along *a* axis which are filled by quinoxalinium cations leading to the formation of the hydrogen bonding interactions. In fact, multiple significant concave red spots appear on the Hirshfeld surface of the anionic units, mapped through d_e function, corresponding to the hydrogen bond interactions C–H···I and N–H···I developed with cationic units and O–H···I created with methanol molecules (see the bottom-right of the colored part in the middle of Fig. S10 and 7c). This result is supported by a quantitative analysis provided by 2D fingerprint plots (FP). In fact, a moderately long and sharp lower spike (where $d_e < d_i$) was found (**2** in Fig. S10), comprising 66.3% of the total Hirshfeld surface area of anionic molecule and emphasizing the acceptor character played by inorganic molecules. The broadness of the spikes **2** may be related to the presence of three different H···I contacts, N–H···I, C–H···I and O–H···I. On the Hirshfeld surface of the adjacent quinoxalinium cations, C–H···I and N–H···I interactions appear as yellow convex spots largely green (see the top-right of the coloured part in the middle of Fig. S10). On the 2D fingerprint plot, the H···I contacts turn up in the upper part of the cationic FP (where $d_e > d_i$), as sharp spike with $d_e + d_i \sim 3.0$ Å, underlining the donor character previously described, with the contribution of 31.5%. As well, N–H···O interaction appears as significant broad convex bright-red depressions, with the contribution of 3.3%. On the 2D fingerprint plot, the H···O contacts turn up in the lower part of the cationic FP (where $d_e < d_i$) as sharp spike with $d_e + d_i \sim 1.6$ Å.

Moreover, a look along the channels shows that the location of the $Qx\text{-}H^+$ cations below each other is mainly due to π···π intermolecular interactions. According to the observation made by Hirshfeld surface mapped with shape index, the presence of π···π stacking is evident by the appearance of red depressions

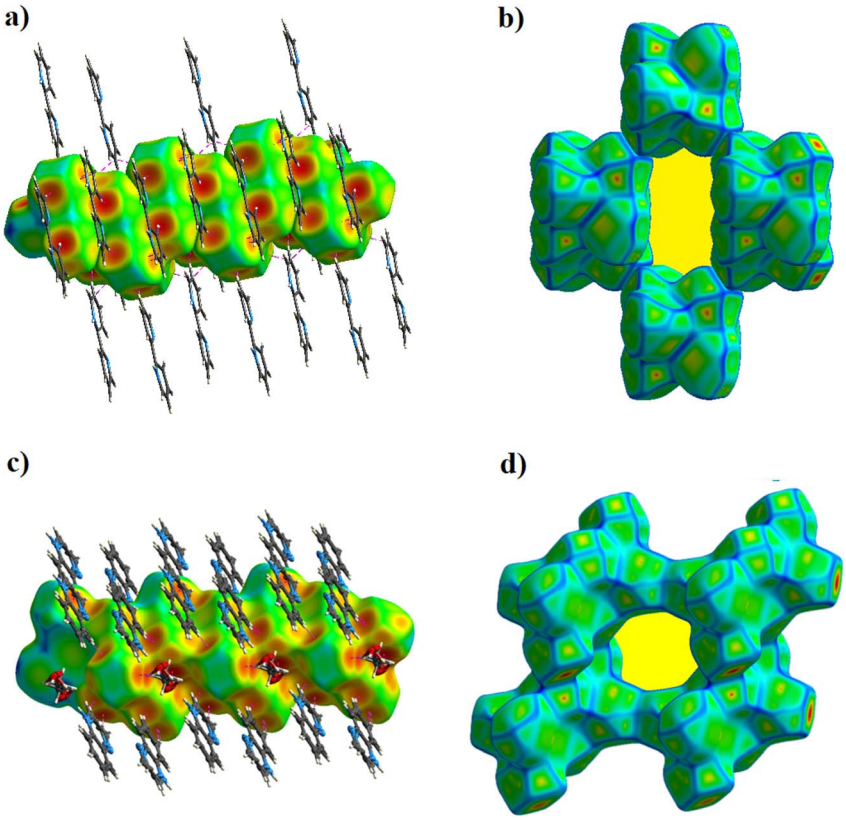

Fig. 7 Hirshfeld surface-packing diagrams of MI_4^- anions mapped over d_e (compound **1** (a) and compound **2** (c)) and over curvedness (compound **1** (b) and compound **2** (d)).

which represent a characteristic of such stacking and a tool that can be used to determine the way in which the molecules overlap and make contact with each other (Fig. S10).

The corresponding fingerprint plot shows this interaction as a region of pale blue/sky blue colour on the diagonal at around $d_e \approx d_i \approx 1.8$ Å, with a contribution of 7.5% of the total Hirshfeld surface area of cationic molecule. Other interactions come into play within organic molecules, C···H/H···C, N···H/H···N and C···N/N···C with the proportions of respectively 20.1, 6.5 and 2.6%.

In addition to that, the crystal structure features significant contribution from I···I interactions in the crystal, with a proportion of 12.9%. As shown in the compound **2**, the importance of such interactions lies in their participation in the formation of a three-dimensional structural framework. As illustrated in Fig. 7d, the blue lines on high curvedness delineate the surface patches that are in contact with adjacent molecules. The curved surface does feature small red spots of low curvedness characteristic of like-atom-like-atom contacts. The presented areas are supportive to the observed intermolecular interactions described in previous sections.

2.4 Vibrational study

In order to verify the functional groups present in the crystals of **1** and **2** and study their vibrational behaviors in the solid state, Raman spectra were recorded in the 50–400 cm^{-1} frequency range, while infrared spectrum were focused between 400 and 4000 cm^{-1}. Both Raman and FT-IR spectra are shown in Fig. 8 and S11–S12, and the frequencies of the observed peaks are cited in Tables S5 and S6.

For compound **1**, the assignment of the bands observed in the region of external modes of the $[SbI_4]^-$ anions (Fig. 8-top) is based on the comparison with the well-documented spectra of the homologous iodoantimonates(III).[63] The Sb–I external stretching vibration, $\nu(Sb–I)_{external}$, gives rise to the strongest Raman line at 156 cm^{-1}. The bands at 126, 112 and 95 cm^{-1} most likely arise from the bridging Sb–I stretch. These stretching vibrations can inform about the presence of $(SbI_4^-)_n$ chains in the structure. Finally, frequencies for the bending modes can be observed in the Raman spectrum between 88 and 55 cm^{-1}. Regarding compound **2**, the Bi–I external stretching vibration, $\nu(Bi–I)_{external}$, gives rise to the stronger Raman line at 141 cm^{-1}. The 122 and 93 cm^{-1} bands arise from the Bi–I bridging stretch ($\nu(Bi–I)_{bridge}$), while the Raman lines at 73 and 55 cm^{-1} correspond to the bending modes.[20,35]

The analysis and the assignment of the internal modes of the 2,2′-bipyridinium cation has been performed by comparison with the spectra of homologous organic–inorganic compounds.[64–66] The infrared spectrum reported in Fig. S11 shows at high wavenumbers two weak bands at 3250 cm^{-1} and 3205 cm^{-1} assignable to NH^+ stretching modes. The weak bands in the 2887–3081 cm^{-1} -range are assigned to ν(C–H) stretching modes. The bands observed between 1249 and

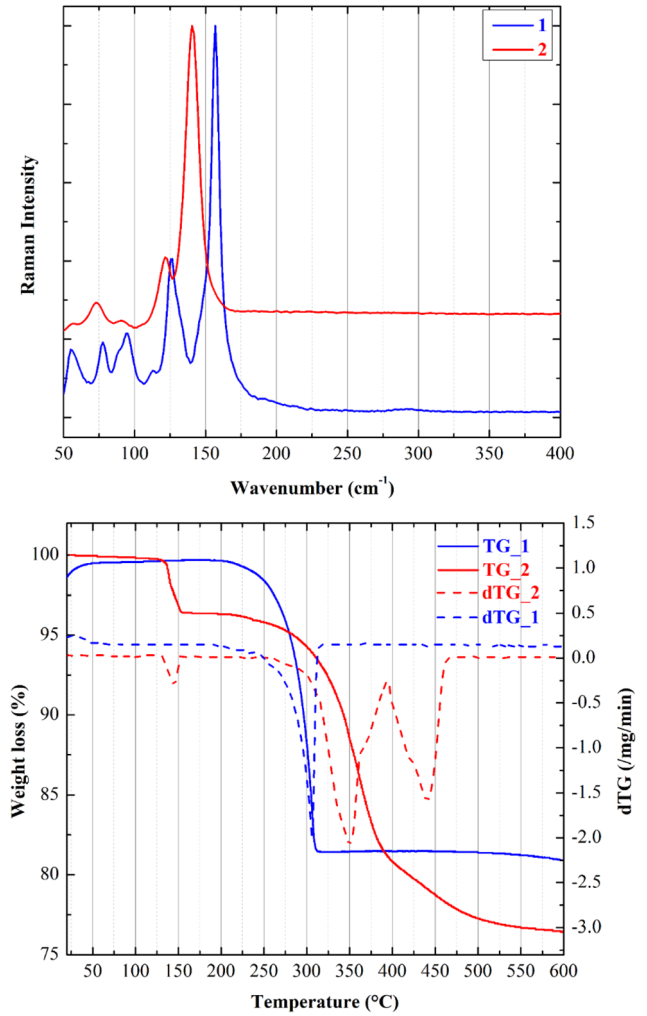

Fig. 8 (Top) Raman spectra of **1** and **2** recorded in the low-frequency range. (Bottom) The TG/DTG spectra of **1** and **2**.

1612 cm^{-1} are attributed to (C=C) and (C=N) ring stretch. The in plane -bending modes of aromatic (C–H) are detected in the region 998–1209 cm^{-1}, while the vibrations at 935, 811 and 761 cm^{-1} are attributed to the out of plane aromatic (C–H) deformation. The bands corresponding to the out of plane deformation on (C=C) and (C=N) are situated at 737 and 718 cm^{-1}. The three bands located at 635, 610 and 542 cm^{-1} are associated with the (CCC) and (CCN) deformation vibration. Finally, the heterocyclic ring torsion appears at 441 cm^{-1}, while the out of plane heterocy-clic ring bending is detected at 423 cm^{-1}.

In the crystal structure of **2**, there is an independent quinoxalinium cation connected to the chlorine atoms by N–$H^{+}\cdots$Cl hydrogen bonds (see Fig. S12 and Table S6). The frequencies assignment observed in the IR spectrum is taken from our previous research on quinoxalinium cation-based halometallates.[21,40,59] The broad band at 3455 cm^{-1} in the IR spectrum is attributed to the O–H stretching mode of the metanol solvent while the two bands observed at 3063 and 3026 cm^{-1} are assigned to the ν(C–H) stretching of the same solvent. Also, the ν(C–O) stretching vibration of methanol appears at 1037 cm^{-1} as an intense peak. The $\nu(NH^{+})$ stretching vibrations of the quinoxalinium cation are observed at 3234 and 3197 cm^{-1} while the bands at 3155 and 3125 cm^{-1} arise from the ν(C–H) stretching vibrations of the quinoxalinium cation. The bands shown at 1615, 1603 and 1566 cm^{-1} originate from the $\nu(C{=}NH^{+})$ stretching vibrations and the ν(C=C) stretching appears between 1517 and 1334 cm^{-1}. The aromatic CCH deformations absorb in the regions 1245–1129 cm^{-1} and 970–906 cm^{-1}. The γ(C=C) coupled with γ(C=N) deformations are observed between 869 and 756 cm^{-1} in the IR spectrum. Finally, the vibrations at 600 and 524 cm^{-1} were associated with the δ(CCN) deformation of the pyridine group and those at 474 and 453 cm^{-1} are due to the δ(CCC) deformation of the aromatic ring.

2.5 Thermal behavior

Fig. 8 (bottom) represents the simultaneous TGA/DTG curves of compounds **1** and **2** recorded at a heating rate of 5 °C min^{-1}. Compound **1** seems to be stable up to about 200 °C and no thermal event was observed before the decomposition of this compound. As shown in the TG curve, the mass loss occurs rapidly during a continuous one-step process in 250–325 °C. However, compound **1** showed a max rate of change of mass of −1.97 mg min^{-1} occurring at 307 °C, which is likely due to the decomposition of the amine.

Compound **2** is quite stable. Indeed, thermal decomposition takes place *via* a first weight loss step of 3.4% that corresponds to the loss of the methanol solvent between 134 and 152 °C (theoritical value 3.7%). A second weight loss step sets in at 228 °C indicating a possible start of sublimation concomitant with additional decomposition reactions (see Fig. 8 bottom). According to DTG data, two mass changes with maximum rates of −2.08 mg min^{-1} and −1.58 mg min^{-1} were observed at 350 °C and 441 °C respectively, which are probably due to the decomposition of amine.

2.6 Absorption and photoluminescence properties

The electronic absorption and emission spectra of compounds **1** and **2** measured using acetonitrile as solvent and in solid-state are shown in Fig. 9–11. Absorption and emission spectral data obtained for compounds **1** and **2** are summarized in Tables 3 and 4, the excitation spectra and radiative decays are reported in Fig. S16–17 and S19–S24, respectively.

In absorption spectrum of compound **1** (Fig. 9A), it can be seen that besides the intense high-energy absorption peaks at 207, 245 and 300 nm owing to the transitions centered on the 2,2′-bipyridinium ion,[67] a low-energy distinct broad band appears between 334 and 500 nm (Fig. 9A), which is very similar to those already published for antimony(III) and bismuth(III) complexes.[68,69] This observed absorption peak at 364 nm, characteristic of the inorganic chains of edge-sharing $[SbI_6]^{3-}$ octahedra, arises from an exciton state formed by the transition from the top of the valence band (VB) consisting of I(5p) orbital to the bottom of the Sb(5p) conduction band (CB). Therefore, this band can be attributed to a halogen-metal charge transfer

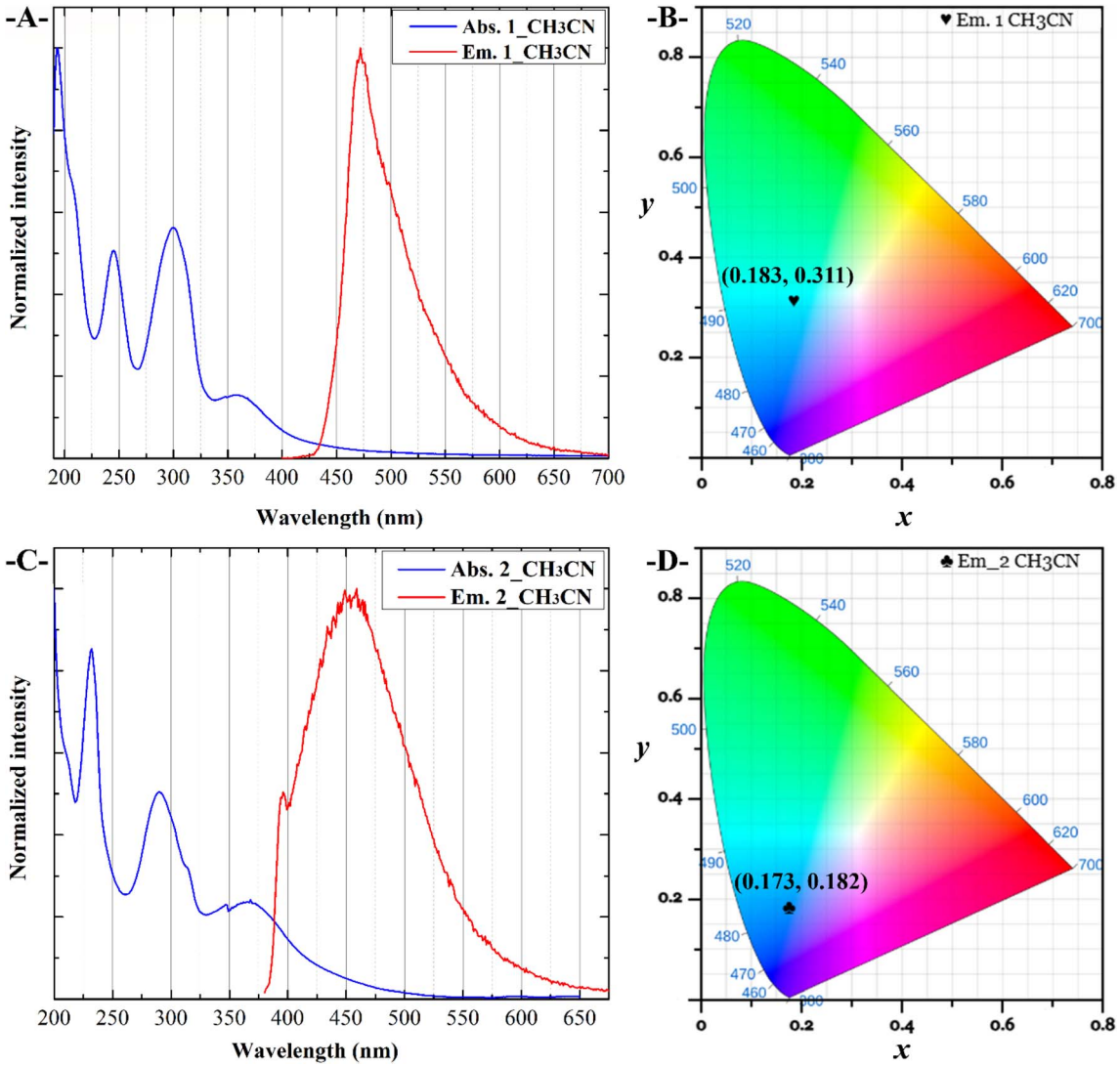

Fig. 9 Normalized absorption and emission spectra of compounds **1** (A) and **2** (C) recorded in CH_3CN at 298 K. Commission Internationale de l'Eclairage (CIE) chromaticity coordinates of **1** (B) and **2** (D) at 298 K.

(XMCT) transition. After excitation at 370 nm, the emission band maximum is observed at 472 nm. This emission can also be attributed to an exciton emission formed during the XMCT transition. This interpretation is consistent with previously reported studies for related antimony(III) and bismuth(III) complexes attributed to XMCT emitters.[68,69] This state is deactivated with quantum yield ($\phi_L = 3.4\%$), and short lifetimes in the nanosecond regime ($\tau = 7.62$ ns).

The absorption spectrum of compound **2** (Fig. 9C) recorded in acetonitrile in comparison with that of the salt (Qx-H)Cl measured under the same conditions (Fig. S18) shows bands between 200 and 330 nm attributed to $\pi \rightarrow \pi^*$ transitions centered on the ligand. Still comparing the absorption spectra of (Qx-H)Cl and compound **2**, we observe the appearance of a new broad band at low energy between 330 and 500 nm which confirms the complexation of the bismuth salt. Moreover, this band exhibits a similar appearance to those observed at low energy for some recently published bismuth iodide complexes based on phenanthroline-derived ligands. Therefore, this band can be also assigned to multiple overlapping electronic transitions due to the ligand-centered LC, the transition halogen to metal center XMCT and metal-centred MC bands. Many works report that bismuth halide complexes are known to exhibit MC and XMCT type bands.[70–72] Following excitation of compound **2** in acetonitrile between 300 and 370 nm, an emission band independent of the excitation wavelength is observed with a maximum at 459 nm. We can note that no emission is observed after excitation between 390 and 500 nm, this suggests the contribution of ligand emission in this band observed for compound **2** (Fig. S18). The quantum yield ($\phi_L = 1.5\%$) and lifetime ($\tau = 2.28$ ns) obtained in solution for compound **2** are very low in comparison with those of the MLCT charge transfer bands observed in coordination polymers (CPs) with bismuth(III) which also corroborates our hypothesis of assignment of the emission band.[73] Moreover, the lifetime measured for the salt (Qx-H)Cl ($\tau = 3.19$ ns) (Fig. S19) is in the same range

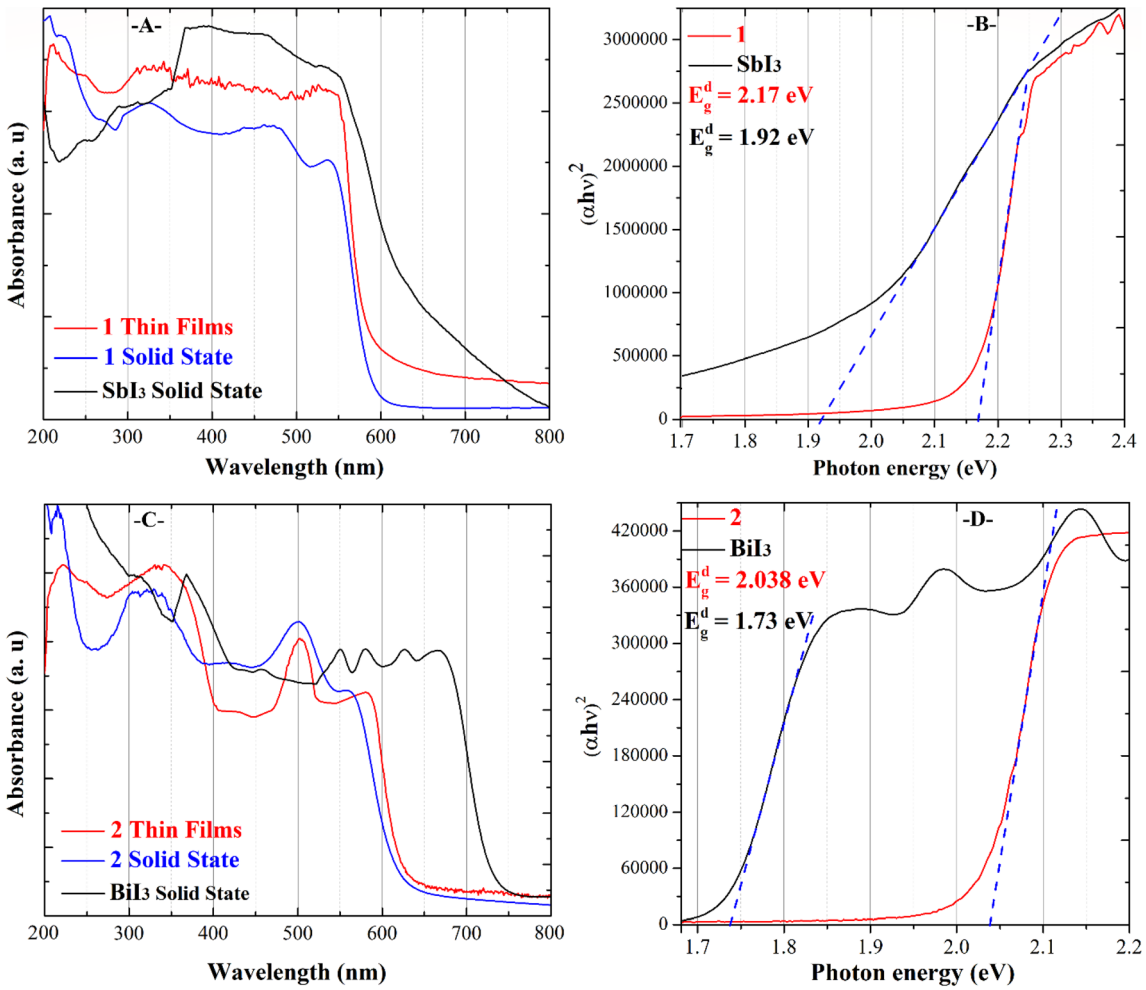

Fig. 10 (A and C) UV-vis absorption spectra of **1**, **2**, SbI_3 and BiI_3 as thin films and powder samples. (B and D) Tauc plot for direct band gap spectra of crystallized films for **1**, **2**, SbI_3 and BiI_3 taken at room temperature; α is the absorption coefficient.

as the complex and thus further confirms the ligand-centered (LC) excited state nature.

In acetonitrile solvent, the chromaticity coordinates (CIE) of **1** and **2** can be tuned from (0.183, 0.311) and (0.46, 0.50), respectively, which corresponds to the blue/green (for **1**) and blue (for **2**) PLs (Fig. 9B and D).

For this study, we were also interested in the photophysical properties of compounds **1** and **2** in the solid state. Optical absorption measurements were carried out for materials **1** and **2** as thin films and powder solid-state samples (Fig. 10A and C), to estimate their optical bandgaps by converting their absorbance spectra into Tauc plots (Fig. 10B and D). It should be noted that the shapes of the optical absorption curves from thin films and from powder solid-state are almost identical. The absorption spectra of the (2-D) starting materials, SbI_3 and BiI_3, are also included in these Figures (black curves) for comparison purposes.

For compound **1**, analysis of the UV/Vis absorption spectrum (Fig. 10A) shows strong absorbance across the ultraviolet and visible region with decreasing intensity up to the absorption edge onsets at 550 nm. The onset of the absorption is significantly blue-shifted relative to that of SbI_3 (Fig. 10A). As shown in Fig. S13, the entire absorption pattern can be decomposed into four Gaussians at about 208 nm (5.96 eV), 339 nm (3.66 eV), 491 nm (2.52 eV) and 543 nm (2.28 eV). The shorter wavelengths peaks are tentatively assigned to π–π^* transitions formed within the organic part,[74] while the peak with maximum at 491 nm, character of the inorganic $(SbI_4^-)_\infty$ chains, can be attributed to the absorption of a highest energetic level in the conduction band.[23] The highest wavelength band at 543 nm is due to band gap absorption and it is assigned to the excitation of free electron–hole pairs within the $(SbI_4)^-$ inorganic chain.

Assuming a direct band gap for this material from the Tauc plot gives E_g value of 2.17 eV (Fig. 10B), which suggests that the material behaves like a semiconductor and is consistent with the orange color of the crystal. The estimated value of the E_g is comparable to other reported optical gaps for low-dimensional (*i.e.*, zero- or one-dimensional) iodoantimonate compounds (~2.13–2.41 eV),[16,32,42,43,75] but very lower than that of 2,2′-bipyridinium based-chloroantimonate compound $(2,2'\text{-bipyH})_4[Sb_4Cl_{20}]$ ($E_g = 3.5$ eV).[74] To our knowledge, the E_g of **1** is alike to

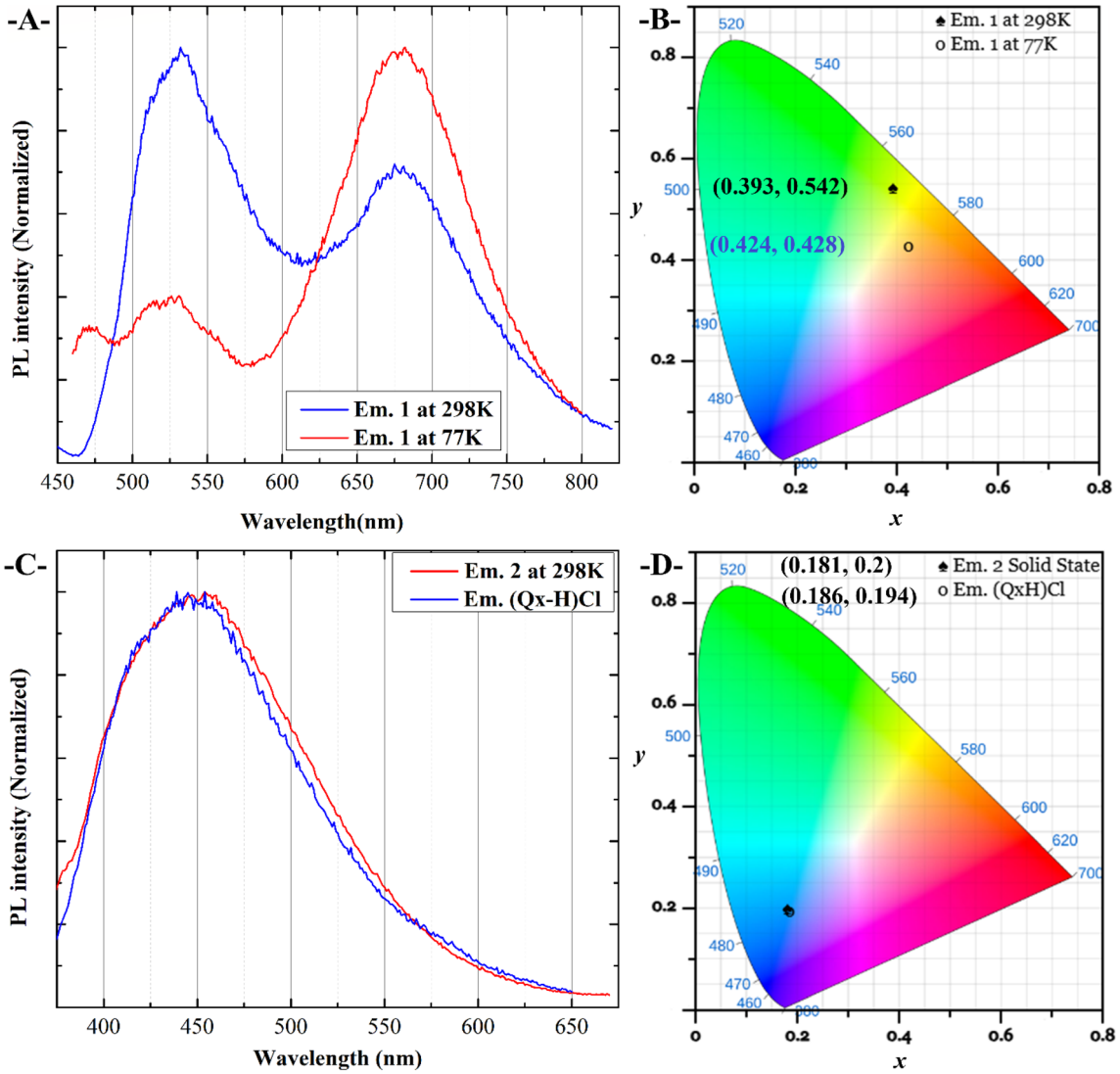

Fig. 11 (A) Normalized solid-state emission spectra **1** recorded at 298 K (blue) and 77 K (red). (B) Commission Internationale de l'Eclairage (CIE) chromaticity coordinates of **1** at 298 K and 77 K. (C) Normalized emission spectra of **2** (red) and (Qx-H)Cl (blue) recorded in solid-state at 298 K. (D) CIE chromaticity coordinates of **2** and (Qx-H)Cl at 298 K.

those of some published Sb-based organic–inorganic materials, which acted as potential light-absorbing materials, such as $(CH_3NH_3)_3Sb_2I_9$ (~2.14 eV),[76] $Cs_3Sb_2I_9$ (~2.03 eV)[77] and $(CH_3NH_3)_2AgSbI_6$ (~1.93 eV).[78] A Tauc plot, assuming an indirect allowed transition, gives an indirect bandgap of 2.038 eV (Fig. S14), slightly lower than the direct bandgap of 2.17 eV. For the starting reagent SbI_3, the estimated band gap is lower in energy (1.92 eV, as seen in Fig. 10B) and is red-shifted relative to material **1**. This result is consistent with the higher dimensionality of the two-dimensional semiconducting starting material relative to the one-dimensional inorganic component of **1**. It is a well-known phenomenon that the band gap of a material rises as it becomes increasingly dimensionally restricted.[13]

Compound **2** shows absorption over most of the visible range (Fig. 10C), with decreasing absorption strength towards its absorption edge onset at 570 nm. This is consistent with its observed dark red coloration. As shown in Fig. 10C, the onset of

Table 3 Absorption and emission data of **1** and **2** in CH_3CN at 298 K

	Absorption	Emission		
Comp.	λ_{abs} (nm) ($\varepsilon \times 10^{-3} M^{-1}$ cm^{-1})	λ_{em} (nm)	ϕ_L (%)	τ(ns)
1	245 (15.8), 300 (17.5), 357 (4.8)	472	3.4	7.62
2	232 (27.9), 290 (19.9), 316 sh (10.1), 368 (8.1)	459	1.5	2.28

Table 4 Emission data of **1** and **2** in solid state at 77 K and 298 K, nd: no determined

Comp.	λ_{em} (nm) at 298 K	λ_{em} (nm) at 77 K	τ(ns) at 298 k
1	537, 681	464, 531, 682	146.32
2	454	nd	3.86

BiI_3 absorption is significantly red-shifted compared to that of compound **2**. The entire absorption pattern for compound **2** (Fig. S15) can be decomposed into four Gaussians at about 216 nm (5.74 eV), 335 nm (3.7 eV), 505 nm (2.45 eV) and 582 nm (2.13 eV). The first two peaks are attributed to π–π^* transitions formed in the organic part, whereas the peak centered at 505 nm can be attributed to an absorption of a highest energetic level occurring on the conduction band. The absorption band at 582 nm is due to band gap absorption and is allotted to an excitation of free electron–hole pairs within the anionic $[BiI_4]^-$ chain.

As shown in Fig. 10D, the optical band gap of **2** was estimated as 2.03 eV, which is nicely consistent with its observed dark red color. The estimated E_g value classifies material **2** as a semiconductor and is comparable to other optical band gaps reported for pseudo-3D iodobismuthate compounds, such as $(NH_2(CH_2)_4NH_2)[BiI_4]_2\cdot 4H_2O$ (~2 eV), $(CH_3NH(CH_2)_4NH_2)[BiI_4]_2\cdot 3H_2O$ (~1.95 eV) $(CH_3NH(CH_2)_4HNCH_3)[BiI_4]_2\cdot 2H_2O$ (~1.92 eV),[79], (pyridinium)BiI_4 (~1.98 eV) and (methylpyridinium)BiI_4 (~2.17 eV).[51] All these pseudo-3D structures exhibit I···I interactions that can subtly modulate the optical band gap towards lower energies than those expected for lower-dimensional structures.[18,19,23] The Tauc plot gives an indirect band gap of 1.912 eV (assuming an allowed indirect transition) which is slightly lower than the direct band gap (2.03 eV) (see Fig. S14). The estimated band gap of the starting material BiI_3 is red-shifted relative to material **2** (1.73 eV; 720 nm) (Fig. 10D), which is consistent with the color (black) and higher dimensionality (2D) of this semiconductor starting material.

The PL spectrum of **1** compound at room temperature (RT) exhibits a dual-emission band; a high-energy (HE) emission at 532 nm (2.33 eV) and a broad low-energy (LE) emission band at 675 nm (1.83 eV) upon the 430 nm irradiation (Fig. 11A). The green emission at 532 nm has a full width at half maximum (FWHM) of 65 nm, whereas the red emission at 675 nm has a width of 150 nm. The profile of the PL suggests that the dual-emission bands for this compound originate from different excited states. The high-energy (HE) emission is almost located at the same wavelength as that of the exciton absorption peak (543 nm) and is therefore assigned to the free excitons (FEs). The low-energy (LE) emission, which significantly increases in intensity at 77 K (see Fig. 11A), may be attributed to self-trapped excitons (STEs) within the distorted inorganic lattices, mediated by strong electron–phonon coupling and defects induced during crystal growth.[19,37,80] This assignment has been validated by numerous previous studies on antimony(III)-based organic–inorganic materials such as α-$[C_6H_4(NH_3)_2]_2Bi_2I_{10}$,[19] $(DMF\text{-}H\text{-}DMF)_2Sb_2I_9$, $(2\text{-pyrr.-}H\text{-}2\text{-pyrr.})_2Sb_2I_8$, $(NMP\text{-}H\text{-}NMP)_3Sb_3I_{12}$,[81] Sb-doped $(DFPD)_2CsBiI_6$ crystals,[82] $(TMEDA)_3Sb_2Br_{12}\cdot H_2O$[83] and $(C_8NH_{12})_4Bi_{0.57}Sb_{0.43}Br_7\cdot H_2O$.[84] Indeed, at 77 K, the HE emission becomes less intense, and the LE emission is enhanced (Fig. 11A), consistent with the population transfer between FEs and STEs at low temperature.[37] We can also note the thermochromism indicated by the appearance of the band at 464 nm at 77 K due to an emission centered on the ligand. It is reported in the literature that some 2D and 1D perovskites emit broadband emission from both FEs and STEs whose generation can be caused by the decrease in dimensionality of perovskites due to strong exciton–phonon interaction.[7,80,85] Therefore, the observed broad emission at 675 nm is attributed to the radiative decay of STEs.[37] Compared with the solid-state emission

Table 5 Crystallographic refinement details for compounds **1** and **2**

Chemical formula	$C_{10}H_9N_2\cdot SbI_4$	$(C_8H_7N_2)_2[BiI_4]_2\cdot CH_3OH$
Formula weight (g mol^{-1})	786.54	1727.51
Crystal system, space group	Monoclinic, *Cc*	Triclinic, $P\bar{1}$
Temperature (K)	100	100
a, *b*, *c* (Å)	12.2685(4), 18.2626(6), 7.5924(3)	7.5699(3), 9.6520(3), 11.5436(6)
α, β, γ (°)	90, 91.864 (1), 90	76.552(2), 86.660(2), 84.383(1)
Volume (Å^3)	1700.21 (10)	815.82 (6)
Z	4	1
Radiation type	Mo Kα	Mo Kα
μ (mm^{-1})	8.87	18.357
Crystal size (mm)	0.22 × 0.19 × 0.17	0.17 × 0.13 × 0.08
Crystal habit	Block/Yellow	Block/Red
Absorption correction	Multi-scan	Multi-scan
Measured reflections	36 006	86 682
Independent reflections	5090	5972
Observed [I > 2σ(I)] reflections	4896	5735
R_{int}	0.027	0.0405
$R[F^2 > 2\sigma(F^2)]$, $wR(F^2)$, S	0.013, 0.028, 1.11	0.0205, 0.0465, 1.058
$\Delta\rho_{max}$, $\Delta\rho_{min}$ (e Å^{-3})	0.50, −0.80	1.59, −1.88

spectrum (observed in Fig. 11A), we observe the disappearance of the line due to STEs (at 675 nm) in the PL spectrum of compound 1 in acetonitrile (Fig. 9A). This is a widely expected phenomenon in such situations. In fact, acetonitrile as a polar solvent can quench the luminescence by affecting the stability of excitons and enhance their tendency to dissociate.[86]

Following excitation at 350 nm of compound **2** in the solid state, an emission band is observed with a maximum at 454 nm (Fig. 11C). In view of the emission obtained for the salt (Qx-H)Cl (Fig. 11C) in the solid state under the same conditions, this band can be unambiguously attributed to a ligand-centered transition. The disappearance of STEs in the PL spectrum may be due to the presence of methanol (polar solvent) in the structure. According to the literature, polar solvents can quench luminescence by increasing the excitons' tendency to dissociate.[86] The lifetime of compound **1** ($\tau = 146.32$ ns) in the solid state is characteristic of the self-trapped excitons (STEs) within the distorted $(SbI_4^-)_\infty$ chains, while that measured for compound **2** ($\tau = 3.86$ ns) is low compared to bismuth(III) complexes,[73] but close to that of the salt (Qx-H)Cl ($\tau = 1.07$ ns) in the solid state (Fig. S20), confirming as previously in solution that this state is centered on the ligand.

The CIE of **1** can be tuned from (0.393, 0.542) to (0.424, 0.428) upon cooling from 298 to 77 °C (Fig. 11B). CIE room temperature chromaticity coordinates are consistent with the yellow/green PL (CCT = 4440 K). Interestingly, **1** has a CIE of (0.424, 0.428) when cooled to 77 K, corresponding to white light with a correlated color temperature (CCT) of 3409 K. Compound **2** shows CIE chromaticity coordinates of (0.181, 0.2) in the color gamut, consistent with the blue PL with a correlated color temperature (CCT) of 1052267 K (Fig. 11D). It is worthwhile pointing out that the (Qx-H)Cl compound has almost the same chromaticity coordinates as those of compound **2** (0.186, 0.194) which is consistent with the blue PL. These results show, unambiguously, that the emissions in **2** and (Qx-H)Cl are caused by the ligand-centered transition.

3. Conclusions

In summary, two organic–inorganic iodometalates, (bpy-H)SbI_4 (**1**) and (Qx-H)$_2[BiI_4]_2\cdot CH_3OH$ (**2**), have been synthesized, by using solvothermal method, with their structures revealed by single-crystal X-ray diffraction. One-dimensional $[MI_4^-]_n$ inorganic chains built by edge-sharing MI_6 octahedra were found in both materials, and the pseudo-3D structures were constructed by connecting these chains *via* I···I interactions. 2,2′-bipyridinium and quinoxalinium cations, for **1** and **2** respectively, were situated in the center of each cavity built by $[MI_4]^-$ chains to balance the charge and stabilize the structures. Analysis of the optical properties revealed that both compounds are semiconductors, with band gaps of around 2.17 eV, for **1**, and 2.03 eV, for **2**. Compound **1** shows dual-band emission which is attributed to the contribution of free excitons and self-trapped excitons, which is evidenced by the long lifetime (146.32 ns) and temperature dependence of the intensity and width of the two emission bands. As for compound **2**, it displays a broad solid-state emission centered at 454 nm, common to the (Qx-H)Cl salt, which confirms the ligand-centered excited state nature. The short lifetimes of compound **2** (3.86 ns) and the (Qx-H)Cl salt (1.07 ns) confirm our findings.

4. Experimental part

All reagents and solvents are commercially available and were used without further purification. Details of the experimental procedures are provided below.

4.1 Preparation of (bpy-H)SbI_4 (1)

SbI_3 (0.5 mmol, 251 mg) and 2,2′-bipyridine (0.5 mmol, 78 mg) were weighed and placed in a 15 mL Teflon lined autoclave with 8 mL acetonitrile as the reaction solvent (Scheme 1). The autoclave was subsequently sealed and heated at a rate of 5 °C min^{-1} to 140 °C. The temperature was held at 140 °C for 102 hours before it was decreased, at a rate of 0.5 °C min^{-1}, to room temperature. Orange block-shaped crystals were isolated from the reaction and a suitable single crystal was selected for the X-ray diffraction experiment. The product yield is calculated to be 85% based on Sb^{3+}. Anal. calcd. for $C_{10}H_9N_2SbI_4$: C, 15.27%; H, 1.15%; N, 3.56%. Found: C, 16.68%; H, 1.04%; N, 3.49%.

4.2 Preparation of (Qx-H)$_2[BiI_4]_2\cdot CH_3OH$ (2)

BiI_3 (0.25 mmol, 147.4 mg) and quinoxaline (0.25 mmol, 32.5 mg) were placed in a 15 mL Teflon-lined autoclave and covered with 8 mL of methanol. 1 mL of concentrated HI was added dropwise to this mixture, and the autoclave was sealed (Scheme 1). The autoclave was then heated at 5 °C min^{-1} to 140 °C and held at this temperature for 50 h before cooling to room temperature at a rate of 0.5 °C min^{-1}. Dark-red block-like crystals of **2** were isolated directly from the reaction, and a suitable single crystal was selected for X-ray crystallographic analysis. Yield is calculated at 78% based on Bi^{3+}. Anal. calcd. for $C_9H_{11}N_2OBiI_4$: C, 12.28%; H, 1.26%; N, 3.18%; O, 1.81%. Found: C, 13.51%; H, 1.18%; N, 3.25%; O, 1.75%.

4.3 Thin films characterization

Thin films of (bpy-H)SbI_4 (**1**) and (Qx-H)$_2[BiI_4]_2\cdot CH_3OH$ (**2**) are prepared following the procedure described in ref. 87. The crystals were mixed with DMF and stirred for 0.5 h to obtain the desired solutions for coating. Then, the films were deposited by the spin coating method (approx. 3000 rev. per min and for 45 s duration) on quartz substrates and were dried at 100 °C for 0.25 h. The thus the prepared films of **1** and **2** were characterized by optical absorbance measurements at room temperature using a UV-vis absorption spectrometer (Hitachi, U-3300).

4.4 Single-crystal X-ray diffraction (SCXRD)

For both compounds **1** and **2**, suitable crystals were selected under a polarizing optical microscope and mounted on a glass fiber for single-crystal X-ray diffraction experiments. X-ray intensity data were collected on a Bruker D8 VENTURE diffractometer using source (Mo-Kα radiation with $\lambda = 0.71073$ Å) at 100 K. The structures solutions were obtained by intrinsic

phasing, developed by successive difference Fourier synthesis, and refined by full-matrix least-squares on all F^2 data using SHELXL and SHELXT programs[88] in a Bruker D8 VENTURE interface. All non-hydrogen atoms were refined anisotropically. The hydrogen atoms were located from difference Fourier maps. Drawings were prepared using the Mercury program.[89]

For compound **2**, the quinoxalinium cation atoms are disordered and split into two sites at 100 K. The occupancies of the corresponding sites are 0.74(4) for major sites and 0.26(4) for minor ones (see Fig. S7). Also, compound **2** exhibits disorder associated with the hydrogen atom responsible for protonation of the quinoxalinium cation. Therefore, this hydrogen was split into two positions (H1 and H1A) with occupancies 0.74(4) and 0.26(4) (Fig. S7). For compound **1** crystallizing in non-centrosymmetric *Cc* space group, the structure could be refined as an inversion twin with a Flack parameter value of 0.45(4).

The crystal data, data collections and structure refinements are summarized in Table 5.

Crystallographic data for the structures of and have been deposited with the Cambridge Crystallographic Data Centre (2494203 for **1** and 2422176 for **2**). Copy of these data can be obtained, free of charge, on application to CCDC, 12 2106560 Union Road, Cambridge CB2 IEZ, UK, fax: 144-(0)1223–336033 or e-mail: deposit@ccdc.cam.ac.uk.

4.5 Powder X-ray diffraction (PXRD)

For PXRD measurements of samples **1** and **2**, a D8 Bruker powder diffractometer, equipped with a front monochromator, was adopted using Cu-Kα radiation ($\lambda = 1.54056$ Å). Powder X-ray diffraction patterns were recorded at room temperature in the 2θ range between 5 and 50°. Experimental and simulated PXRD patterns from single crystal data were compared to confirm phases homogeneity.

4.6 Infrared (FT-IR) and Raman spectroscopy

The infrared spectra have been recorded on a PerkinElmer Spectrum 100 FT-IR spectrometer with KBr pellet in the range 4000–400 cm^{-1}. The Raman spectra has been recorded on a HORIBA JOBIN-YVON (T64000) spectrometer and excited at 633 nm. The laser beam was focused onto the sample through a 50× microscope objective and the power limited to 5 mW to avoid sample heating.

4.7 Thermogravimetric analysis (TGA)

The thermal behavior of **1** and **2**, was performed on a "Setaram SETSYS 16/18" instrument between 25 and 600 °C with a ramp rate of 5 °C min^{-1}. The scans were performed under flowing argon.

4.8 Differential scanning calorimetry (DSC)

DSC analysis was performed with a DSC 822P METTLER TOLEDO instrument at temperatures ranging from −90 to 20 °C, at a rate of 5 °C min^{-1} during cooling and heating. Analysis was carried out in a nitrogen atmosphere.

4.9 UV-vis and photoluminescence

Diffuse reflectance UV-visible spectroscopy measurements for compounds **1**, **2**, SbI_3 and BiI_3 were made on polycrystalline samples using Shimadzu (UV-3101 PC UV-Vis-NIR) spectrophotometer. An integrating optical sphere is employed to collect the diffuse light at room temperature in the spectral range of 200–800 nm.

UV-vis spectra were measured in CH_3CN with a VARIAN-Cary 300 spectrophotometer and emission spectra were recorded on a Jobin-Yvon Fluoro log 3 in CH_3CN at rt and in solid-state at rt and 77 K. Luminescence quantum yields ϕ_L of complexes at 298 K were determined using anthracene ($\phi_L = 27\%$) as a luminescence quantum yield standard.[90] Luminescence lifetimes were obtained using a Horiba Jobin-Yvon FL-R928P-TCSPC apparatus equipped with a deltadiode (350 nm) source. The lifetimes of compounds **1** and **2** in solution and in the solid state were measured at the emission maxima. Analysis of luminescence decay profiles against time was accomplished using the Decay Analysis Software DAS6.

4.10 Hirshfeld surface (HS) calculation

Hirshfeld molecular surfaces for both compounds were generated using the Crystal Explorer 21 program,[91] which is a valuable and complementary visual tool of exploring and analysing intermolecular interactions in molecular crystals while maintaining a whole-of-molecule approach.[92] Two parameters are defined for each point on the Hirshfeld surface: d_e and d_i, distances from the surface to the nearest nucleus exterior and interior to the surface, respectively. Then four different functions mapped in colour on the Hirshfeld surface have been explored in this work. The normalized contact distance, d_{norm}, is displayed using a red-white-blue color scheme and its value is negative (red regions) and positive (blue region) for contacts shorter and greater than vdW separations, respectively. Moreover, maps of shape index, S, on the Hirshfeld surface can be used to identify complementary hollows (red regions) and bumps (blue regions) where two molecular Hirshfeld surfaces touch one another. The distance external to the surface, d_e, measures the distance from the surface to the nearest nucleus in another molecule. It provides an excellent and immediate picture of close intermolecular contacts. Finally, the maps of curvedness, C, delineate the areas on the surface that represent close contact between two molecular Hirshfeld surfaces, and hence enable us to extract information about the number of nearest neighbours or the coordination sphere of each molecule.

Author contributions

CH: conceptualization, methodology, analysis of the data, writing – original draft, review & editing; MH: preparation of the compounds, calculations using crystal explorer, generation of images, writing of the paper; ME: preparation of the compounds; MN and AK: UV-vis and photoluminescence measurements; MK: validation, review & editing; LV: PXRD

measurements; AS and CS: collection of X-ray data and structure resolution; SC: validation, formal analysis.

Conflicts of interest

There are no conflicts to declare.

Note added after first publication

This article replaces the version published on 7th November 2025. A small number of layout concerns, typographical errors and grammatical points have been corrected and the Acknowledgements section has been included. No changes have been made to the scientific content.

Data availability

The data recorded in this manuscript are available upon request.

CCDC 2494203 (**1**) and 2422176 (**2**) contain the supplementary crystallographic data for this paper.[93a,b]

Supplementary information: PXRD, DSC, FT-IR, UV-vis spectra, excitation spectra, emission decay, pictures of crystal structures and Hirshfeld surface analysis. Tables of interatomic distances, Hydrogen-bond geometries and frequencies of Raman and infrared bands. See DOI: **https://doi.org/10.1039/d5ra06189j**.

Acknowledgements

We thank Fonds der Chemischen Industrie and Studienstiftung des deutschen Volkes for financial support through a scholarship to AS.

References

1 A. K. Jena, A. Kulkarni and T. Miyasaka, *Chem. Rev.*, 2019, **119**, 3036–3103, DOI: **10.1021/acs.chemrev.8b00539**.
2 C. Zhou, H. Lin, Y. Tian, Z. Yuan, R. Clark, B. Chen, L. J. van de Burgt, J. C. Wang, Y. Zhou, K. Hanson, Q. J. Meisner, J. Neu, T. Besara, T. Siegrist, E. Lambers, P. Djurovich and B. Ma, *Chem. Sci.*, 2018, **9**, 586–593, DOI: **10.1039/C7SC04539E**.
3 S. Yakunin, D. N. Dirin, Y. Shynkarenko, V. Morad, I. Cherniukh, O. Nazarenko, D. Kreil, T. Nauser and M. V. Kovalenko, *Nat. Photonics*, 2016, **10**, 585–589, DOI: **10.1038/nphoton.2016.139**.
4 C. R. Kagan, D. B. Mitzi and C. D. Dimitrakopoulos, *Science*, 1999, **286**, 945–947, DOI: **10.1126/science.286.5441.945**.
5 J. Burschka, N. Pellet, S.-J. Moon, R. Humphry-Baker, P. Gao, M. K. Nazeeruddin and M. Gratzel, *Nature*, 2013, **499**, 316–319, DOI: **10.1038/nature12340**.
6 E. P. Booker, T. H. Thomas, C. Quarti, M. R. Stanton, C. D. Dashwood, A. J. Gillett, J. M. Richter, A. J. Pearson, N. J. L. K. Davis, H. Sirringhaus, M. B. Price, N. C. Greenham, D. Beljonne, S. E. Dutton and F. Deschler, *Am. Chem. Soc.*, 2017, **139**, 18632–18639, DOI: **10.1021/jacs.7b10223**.
7 Z. Yuan, C. Zhou, Y. Tian, Y. Shu, J. Messier, J. C. Wang, L. J. van de Burgt, K. Kountouriotis, Y. Xin, E. Holt, K. Schanze, R. Clark, T. Siegrist and B. Ma, *Nat. Commun.*, 2017, **8**, 14051, DOI: **10.1038/ncomms14051**.
8 B.-W. Park, B. Philippe, X. Zhang, H. Rensmo, G. Boschloo and E. M. J. Johansson, *Adv. Mater.*, 2015, **27**, 6806, DOI: **10.1002/adma.201501978**.
9 D. M. Griffith, H. Li, M. V. Werrett, P. C. Andrews and H. Sun, *Chem. Soc. Rev.*, 2021, **50**, 12037, DOI: **10.1039/D0CS00031K**.
10 J. Li, H.-L. Cao, W.-B. Jiao, Q. Wang, M. Wei, I. Cantone, J. Lü and A. Abate, *Nat. Commun.*, 2020, **11**, 310, DOI: **10.1038/s41467-019-13910-y**.
11 A. García-Fernández, I. Marcos-Cives, C. Platas-Iglesias, S. Castro-García, D. Vázquez-García, A. Fernández and M. Sánchez-Andújar, *Inorg. Chem.*, 2018, **57**, 7655–7664, DOI: **10.1021/acs.inorgchem.8b00629**.
12 P. Hao, W. Wang, J. Shen and Y. Fu, *Dalton Trans.*, 2020, **49**, 1847–1853, DOI: **10.1039/C9DT04818A**.
13 Z. Shi, J. Guo, Y. Chen, Q. Li, Y. Pan, H. Zhang, Y. Xia and W. Huang, *Adv. Mater.*, 2017, **29**, 1605005, DOI: **10.1002/adma.201605005**.
14 J. Shin, M. Kim, S. Jung, C. S. Kim, J. Park, A. Song, K.-B. Chung, S.-H. Jin, J. H. Lee and M. Song, *Nano Res.*, 2018, **11**, 6283–6293, DOI: **10.1007/s12274-018-2151-4**.
15 Z. Xiao, W. Meng, J. Wang, D. B. Mitzi and Y. Yan, *Mater. Horiz.*, 2017, **4**, 206–216, DOI: **10.1039/C6MH00519E**.
16 J. Möbs, G. Stuhrmann, F. Weigend and J. Heine, *Chem.–Eur. J.*, 2023, **29**, e202202931, DOI: **10.1002/chem.202202931**.
17 C. Hrizi, C. Chaker and S. Chaabouni, *Ionics*, 2011, **17**, 545–553, DOI: **10.1007/s11581-011-0558-y**.
18 C. Hrizi, A. Samet, Y. Abid, S. Chaabouni, M. Fliyou and A. Koumina, *J. Mol. Struct.*, 2011, **992**, 96–101, DOI: **10.1016/j.molstruc.2011.02.051**.
19 C. Hrizi, A. Trigui, Y. Abid, N. C-Boudjada, P. Bordet and S. Chaabouni, *J. Solid State Chem.*, 2011, **184**, 3336–3344, DOI: **10.1016/J.JSSC.2011.10.004**.
20 M. Essid, C. Hrizi, S. Ammar, A. Khatyr, M. Knorr, A. Schmidt and C. Strohmann, *Molbank*, 2024, **2024**, M1755, DOI: **10.3390/M1755**.
21 S. Jarboui, C. Hrizi, A. Ben Ahmed, M. Knorr, A. Schmidt, C. Strohmann and F. Zouari, *J. Molec. Struct.*, 2025, **1338**, 142329, DOI: **10.1016/j.molstruc.2025.142329**.
22 Y. Li, Z. Xu, X. Liu, K. Tao, S. Han, Y. Wang, Y. Liu, M. Li, J. Luo and Z. Sun, *Inorg. Chem.*, 2019, **58**, 6544–6549, DOI: **10.1021/acs.inorgchem.9b00718**.
23 C. Hrizi, N. Chaari, Y. Abid, N. Chniba-Boudjada and S. Chaabouni, *Polyhedron*, 2012, **46**, 41–46, DOI: **10.1016/j.poly.2012.07.062**.
24 C. Hrizi and S. Chaabouni, *Jpn. Soc. Anal. Chem.*, 2010, **26**, 3–4, DOI: **10.2116/xraystruct.26.3**.
25 D. M. Fabian and S. Ardo, *J. Mater. Chem. A*, 2016, **4**, 6837–6841, DOI: **10.1039/c6ta00517a**.
26 S. Pohl, M. Peters, D. Haase, W. Saak and Z. Naturforsch, *B: J. Chem. Sci.*, 1994, **49b**, 741–746, DOI: **10.1515/znb-1994-0604**.

27 A. M. Goforth, L. Peterson Jr, M. D. Smith and H.-C. zur Loye, *J. Solid State Chem.*, 2005, **178**, 3529–3540, DOI: 10.1016/j.jssc.2005.09.010.
28 D. B. Mitzi, *Inorg. Chem.*, 2000, **39**, 6107–6113, DOI: 10.1021/ic000794i.
29 G. C. Papavassiliou, *Prog. Solid State Chem.*, 1997, **25**, 125, DOI: 10.1016/S0079-6786(97)80886-2.
30 E. G. Tulsky and J. R. Long, *Chem. Mater.*, 2001, **13**, 1149, DOI: 10.1021/cm0007858.
31 G. A. Fisher and N. C. Norman, *Adv. Inorg. Chem.*, 1994, **41**, 233–271, DOI: 10.1016/S0898-8838(08)60173-7.
32 G. A. Mousdis, N.-M. Ganotopoulos, H. Barkaoui, Y. Abid, V. Psycharis, A. Savvidou and C. P. Raptopoulou, *Eur. J. Inorg. Chem.*, 2017, **2017**, 3401, DOI: 10.1002/ejic.201700277.
33 P.-F. Li, Y.-Y. Tang, W.-Q. Liao, H.-Y. Ye, Y. Zhang, D.-W. Fu, Y.-M. You and R.-G. Xiong, *NPG Asia Mater.*, 2017, **9**, e342, DOI: 10.1038/am.2016.193.
34 J.-X. Gao, X.-N. Hua, X.-G. Chen, G.-Q. Mei and W.-Q. Liao, *Inorg. Chem.*, 2019, **58**, 4337, DOI: 10.1021/acs.inorgchem.8b03424.
35 Y. Li, T. Yang, X. Liu, S. Han, J. Wang, Y. Ma, W. Guo, J. Luo and Z. Sun, *Inorg. Chem. Front.*, 2020, **7**, 2770, DOI: 10.1039/D0QI00546K.
36 R. Zhang, X. Mao, Y. Yang, S. Yang, W. Zhao, T. Wumaier, D. Wei, W. Deng and K. Han, *Angew. Chem., Int. Ed.*, 2019, **58**, 2725–2729, DOI: 10.1002/anie.201812865.
37 M. K. Jana, R. Song, H. Liu, D. R. Khanal, S. M. Janke, R. Zhao, C. Liu, Z. V. Vardeny, V. Blum and D. B. Mitzi, *Nat. Commun.*, 2020, **11**, 4699, DOI: 10.1038/s41467-020-18485-7.
38 A. M. Goforth, M. A. Tershansy, M. D. Smith, L. Peterson Jr and H.-C. zur Loye, *Acta Cryst.*, 2006, **C62**, m381–m385, DOI: 10.1107/S0108270106025972.
39 C. J. Carmalt, L. J. Farrugia and N. C. Norman, *Z. anorg. allg. Chem.*, 1995, **621**, 47–56, DOI: 10.1002/zaac.19956210110.
40 M. Hamdouni, C. Hrizi, H. E. Ahmed, M. Knorr, A. Krupp, C. Strohmann and S. Chaabouni, *J. Mol. Struct.*, 2023, **1274**, 134590, DOI: 10.1016/j.molstruc.2022.134590.
41 M. Bujak, *Acta Cryst.*, 2017, **B73**, 432–442, DOI: 10.1107/S2052520617003420.
42 A. J. Dennington and M. Weller, *Dalton Trans.*, 2018, **47**, 3469–3484, DOI: 10.1039/C7DT04280A.
43 A. Gągor, G. Banach, M. Węcławik, A. Piecha-Bisiorek and R. Jakubas, *Dalton Trans.*, 2017, **46**, 16605–16614, DOI: 10.1039/C7DT03622A.
44 Y.-Q. Hu, H.-Y. Hui, W.-Q. Lin, H.-Q. Wen, D.-S. Yang and G.-D. Feng, *Inorg. Chem.*, 2019, **58**, 16346–16353, DOI: 10.1021/acs.inorgchem.9b01439.
45 I. W. H. Oswald, E. M. Mozur, I. P. Moseley, H. Ahn and J. R. Neilson, *Inorg. Chem.*, 2019, **58**, 5818–5826, DOI: 10.1021/acs.inorgchem.9b00170.
46 I. D. Brown, *J. Solid State Chem.*, 1974, **11**, 214–233, DOI: 10.1016/S0022-4596(74)80006-X.
47 R. D. Shannon, *Acta Crystallogr.*, 1976, **A32**, 751, DOI: 10.1107/S0567739476001551.
48 F. Van Bolhuis, P. B. Koster and T. Migchelsen, *Acta Cryst*, 1967, **23**, 90–91, DOI: 10.1107/S0365110X6700218X.
49 D. B. Mitzi and P. Brock, *Inorg. Chem.*, 2001, **40**, 2096–2104, DOI: 10.1021/ic000622l.
50 Y. Wang, R. Wen, Y. Liu, L.-Y. Bi, M. Yang, H. Sun, Y.-Z. Zheng, G. Zhang and Z. Gao, *ChemSusChem*, 2020, **13**, 2753–2760, DOI: 10.1002/cssc.202000282.
51 T. Li, Y. Hu, C. A. Morrison, W. Wu, H. Han and N. Robertson, *Sustainable Energy Fuels*, 2017, **1**, 308–316, DOI: 10.1039/C6SE00061D.
52 M. D. Petrov, M. N. Sokolov, V. P. Fedin and S. A. Adonin, *J. Struct. Chem.*, 2020, **61**, 1794–1799, DOI: 10.1134/S0022476620110128.
53 A. Lipka, *Z. Naturforsch. B*, 1983, **38**, 1615–1621, DOI: 10.1515/znb-1983-1213.
54 G. A. Bowmaker, P. C. Junk, A. M. Lee, B. W. Skelton and A. H. White, *Aust. J. Chem.*, 1998, **51**, 293, DOI: 10.1071/C97036.
55 G. Alonzo, F. Benetollo, N. Bertazzi and G. Bombieri, *J. Chem. Crystallogr.*, 1999, **29**, 913–919, DOI: 10.1023/A:1009578028913.
56 A. Angeloni, P. C. Crawford, A. G. Orpen, T. J. Podesta and B. J. Shore, *Chem.–Eur. J.*, 2004, **10**, 3783–3791, DOI: 10.1002/chem.200400165.
57 M. Nunn, A. J. Blake, M. J. Begley and D. B. Sowerby, *Polyhedron*, 1998, **17**, 4213–4217, DOI: 10.1016/S0277-5387(98)00231-9.
58 S. Chaabouni, S. Kamoun and J. Jaud, *J. Chem. Crystallogr.*, 1997, **27**, 527–531, DOI: 10.1007/BF02576443.
59 S. Jarboui, C. Hrizi, A. Oueslati and F. Zouari, *Inorganica chem. Acta.*, 2024, **561**, 121876, DOI: 10.1016/j.ica.2023.121876.
60 I. Cvrtila and V. Stilinovic, *Cryst. Growth Des.*, 2017, **17**, 6793–6800, DOI: 10.1021/acs.cgd.7b01363.
61 J. J. Mckinnon, M. A. Spackman and A. S. Mitchell, *Acta. Cryst.*, 2004, **B60**, 627–668, DOI: 10.1107/S0108768104020300.
62 K. Gholivand, F. Molaej, M. Rajabi, M. D. Esrafili and M. Hosseini, *Polyhedron*, 2014, **71**, 8–16, DOI: 10.1016/j.poly.2014.01.001.
63 P. W. Jagodzinski and J. Laane, *J. Raman Spectrosc.*, 1980, **9**, 22–27, DOI: 10.1002/jrs.1250090107.
64 E. P. S. Martins, G. B. Rocha, J. de A. Simoni and J. G. de P. Espínola, *Thermochim. Acta*, 2019, **676**, 234–240, DOI: 10.1016/j.tca.2019.05.005.
65 E. König and E. Lindner, *Spectrochim. Acta, Part A*, 1972, **28**, 1393–1403, DOI: 10.1016/0584-8539(72)80108-9.
66 T. P. Gerasimova and S. A. Katsyuba, *Dalton Trans.*, 2013, **42**, 1787–1797, DOI: 10.1039/C2DT31922E.
67 D. Zhang, J. P. Telo, C. Liao, S. E. Hightower and E. L. Clennan, *J. Phys. Chem. A*, 2007, **111**, 13567–13574, DOI: 10.1021/jp074323u.
68 H. Bhatia, J. Guo, C. N. Savory, M. Rush, D. I. James, A. Dey, C. Chen, D.-K. Bucar, T. M. Clarke, D. O. Scanlon, R. G. Palgrave and B. C. Schroeder, *Inorg. Chem.*, 2024, **63**, 416–430, DOI: 10.1021/acs.inorgchem.3c03290.
69 H. Nikol and A. Vogler, *J. Am. Chem. Soc.*, 1991, **113**, 8988–8990, DOI: 10.1021/ja00023a081.

70 E. H. Choi, D.-S. Ahn, S. Park, C. Kim, C. W. Ahn, S. Kim, M. Choi, C. Yang, T. W. Kim, H. Ki, J. Choi, M. N. Pedersen, M. Wulff, J. Kim and H. Ihee, *J. Phys. Chem. Lett.*, 2019, **10**, 1279–1285, DOI: **10.1021/acs.jpclett.9b00365**.

71 O. Horváth and I. Mikó, *Inorg. Chim. Acta*, 2000, **304**, 210–218, DOI: **10.1016/S0020-1693(00)00090-6**.

72 F. T. Gemeda, V. Vorobyev and A. N. Tarnovsky, *J. Phys. Chem. B*, 2022, **126**, 1254–1267, DOI: **10.1021/acs.jpcb.1c10350**.

73 J. R. Sorg, T. Wehner, P. R. Matthes, R. Sure, S. Grimme, J. Heine and K. Müller-Buschbauma, *Dalton Trans.*, 2018, **47**, 7669–7681, DOI: **10.1039/c8dt00642c**.

74 E. Toumi, O. Kammoun, N. Elleuch and M. Boujelbene, *J. Molec. Struct.*, 2024, **1299**, 137238, DOI: **10.1016/j.molstruc.2023.137238**.

75 N. Dehnhardt, M. Axt, J. Zimmermann, M. Yang, G. Mette and J. Heine, *Chem. Mater.*, 2020, **32**, 4801–4807, DOI: **10.1021/acs.chemmater.0c01605**.

76 J.-C. Hebig, I. Kühn, J. Flohre and T. Kirchartz, *ACS Energy Lett.*, 2016, **1**, 309–314, DOI: **10.1021/acsenergylett.6b00170**.

77 A. Singh, K. M. Boopathi, A. Mohapatra, Y. F. Chen, G. Li and C. W. Chu, *ACS Appl. Mater. Interfaces*, 2018, **10**, 2566–2573, DOI: **10.1021/acsami.7b16349**.

78 Y. J. Li, T. Wu, L. Sun, R. X. Yang, L. Jiang, P. F. Cheng, Q. Q. Hao, T. J. Wang, R. F. Lu and W. Q. Deng, *RSC Adv.*, 2017, **7**, 35175–35180, DOI: **10.1039/C7RA06130G**.

79 A. J. Dennington and M. Weller, *Dalton Trans.*, 2016, **45**, 17974–17979, DOI: **10.1039/C6DT03602C**.

80 M. D. Smith and H. I. Karunadasa, *Acc. Chem. Res.*, 2018, **51**, 619–627, DOI: **10.1021/acs.accounts.7b00433**.

81 S. Parmar, S. Pal, A. Biswas, S. Gosavi, S. Chakraborty, M. C. Reddy and S. Ogale, *Chem. Commun.*, 2019, **55**, 7562–7565, DOI: **10.1039/C9CC03485D**.

82 T. Bai, X. Wang, Y. He, H. Wei, Y. Su and J. Chen, *Adv. Optical Mater.*, 2023, **11**, 2301110, DOI: **10.1002/adom.202301110**.

83 C. Deng, S. Hao, K. Liu, M. S. Molokeev, C. Wolverton, L. Fan, G. Zhou, D. Chen, J. Zhao and Q. Liu, *J. Mater. Chem. C*, 2021, **9**, 15942–15948, DOI: **10.1039/d1tc04198c**.

84 R. Zhang, X. Mao, Y. Yang, S. Yang, W. Zhao, T. Wumaier, D. Wei, W. Deng and K. Han, *Angew. Chem., Int. Ed.*, 2019, **58**, 2725–2729, DOI: **10.1002/anie.201812865**.

85 D. Cortecchia, J. Yin, A. Bruno, S. Z. A. Lo, G. G. Gurzadyan, S. Mhaisalkar, J. L. Brédas and C. Soci, *J. Mater. Chem. C*, 2017, **5**, 2771–2780, DOI: **10.1039/C7TC00366H**.

86 G. Cao and Y. Wang, *Nanostructures and Nanomaterials: Synthesis, Properties and Applications*, Imperial College Press (distributed by World Scientific), London, 2004, ISBN 1-86094-415-9.

87 M. Hamdouni, C. Hrizi, M. O. M. Esghaier, M. Knorr, C. Strohmann and S. Chaabouni, *CrystEngComm*, 2024, **26**, 2723–2736, DOI: **10.1039/d4ce00079j**.

88 G. M. Sheldrick, *Acta Crystallogr., Sect. A:Found. Adv.*, 2015, **71**, 3–8, DOI: **10.1107/S2053273314026370**.

89 C. F. Macrae, I. Sovago, S. J. Cottrell, P. T. A. Galek, P. McCabe, E. Pidcock, M. Platings, G. P. Shields, J. S. Stevens, M. Towler and P. A. Wood, *J. Appl. Cryst.*, 2020, **53**, 226–235, DOI: **10.1107/S1600576719014092**.

90 W. H. Melhuish, *J. Phys. Chem.*, 1961, **65**, 229–235.

91 P. R. Spackman, M. J. Turner, J. J. McKinnon, S. K. Wolff, D. J. Grimwood, D. Jayatilaka and M. A. Spackman, *J. Appl.Crystallogr.*, 2021, **54**, 1006–1011, DOI: **10.1107/S1600576721002910**.

92 J. J. McKinnon, D. Jayatilaka and M. A. Spackman, *Chem. Commun.*, 2007, 3814–3816, DOI: **10.1039/b704980c**.

93 (*a*) CCDC 2494203: Experimental Crystal Structure Determination, 2025, DOI: **10.5517/ccdc.csd.cc2pqf51**; (*b*) CCDC 2422176: Experimental Crystal Structure Determination, 2025, DOI: **10.5517/ccdc.csd.cc2m9gq4**.